Received: 16 December 2020 | Revised: 8 June 2021 | Accepted: 27 July 2021

DOI: 10.1002/qj.4142

Quarterly Journal of the Royal Meteorological Society RMetS

RESEARCH ARTICLE

The impact of Aeolus wind retrievals on ECMWF global weather forecasts

Michael P. Rennie[1] | **Lars Isaksen**[1] | **Fabian Weiler**[2] | **Jos de Kloe**[3] | **Thomas Kanitz**[4] | **Oliver Reitebuch**[2]

[1]European Centre for Medium-Range Weather Forecasts, Reading, UK

[2]Deutsches Zentrum für Luft- und Raumfahrt e.V. (DLR), Institut für Physik der Atmosphäre, Oberpfaffenhofen, Germany

[3]Royal Netherlands Meteorological Institute (KNMI), De Bilt, The Netherlands

[4]European Space Agency (ESA/ESTEC), Noordwijk, The Netherlands

Correspondence
M.P. Rennie, European Centre for Medium-Range Weather Forecasts, Shinfield Park, Reading RG2 9AX, UK.
Email: m.rennie@ecmwf.int

Abstract

Aeolus is the world's first spaceborne Doppler Wind Lidar, providing profiles of horizontal line-of-sight (HLOS) wind retrievals. Numerical weather prediction (NWP) impact and error statistics of Aeolus Level-2B (L2B) wind statistics have been assessed using the European Centre for Medium-range Weather Forecasts (ECMWF) global data assimilation system. Random and systematic error estimates were derived from observation minus background departure statistics. The HLOS wind random error standard deviation is estimated to be in the range 4.0–7.0 $m \cdot s^{-1}$ for the Rayleigh-clear and 2.8–3.6 $m \cdot s^{-1}$ for the Mie-cloudy, depending on atmospheric signal levels which in turn depend on instrument performance, atmospheric backscatter properties and the processing algorithms. Complex systematic HLOS wind error variations on time-scales less than one orbit were identified, most strongly affecting the Rayleigh-clear winds. NWP departures and instrument housekeeping data confirmed that it is caused by temperature gradients across the primary mirror. A successful bias correction scheme was implemented in the operational processing chain in April 2020. In Observing System Experiments (OSEs), Aeolus provides statistically significant improvement in short-range forecasts as verified by observations sensitive to temperature, wind and humidity. Longer forecast range verification shows positive impact that is strongest at the day two to three forecast range: ~2% improvement in root-mean-square error for vector wind and temperature in the tropical upper troposphere and lower stratosphere, and polar troposphere. Positive impact up to 9 days is found in the tropical lower stratosphere. Both Rayleigh-clear and Mie-cloudy winds provide positive impact, but the Rayleigh accounts for most tropical impact. The Forecast Sensitivity Observation Impact (FSOI) metric is available since 9 January 2020, when Aeolus was operationally assimilated, which confirms Aeolus is a useful contribution to the global observing system, with the Rayleigh-clear and Mie-cloudy winds providing similar overall short-range impact in 2020.

KEYWORDS

Aeolus, assimilation, Doppler Wind Lidar, numerical weather prediction, NWP impact, observation biases and errors, observations

1 | INTRODUCTION

This article concerns the use of the novel wind profiles from the Aeolus satellite mission (ESA, 2008; Straume *et al.*, 2020) in global numerical weather prediction (NWP), in particular the Level-2B (L2B) HLOS (horizontal line-of-sight) wind data. We assessed the quality of Aeolus wind retrievals and their impact on global NWP using the European Centre for Medium-range Weather Forecasts (ECMWF) system.

In 2018 the World Meteorological Organisation (WMO) Rolling Review of Requirements (WMO, 2018) listed wind profiles as the highest priority critical atmospheric variable not being adequately measured by the global observing systems. Aeolus partially fills this wind data gap and it is of great interest to evaluate its NWP impact to demonstrate the potential value of future wind lidar missions. Many studies have investigated the potential benefits of more wind profile observations for NWP, such as: Stoffelen *et al.*, 2006; 2020a; Tan *et al.*, 2007; Weissmann and Cardinali, 2007; Marseille *et al.*, 2008; Baker *et al.*, 2014; Horányi *et al.*, 2015a; Illingworth *et al.*, 2018. These theoretical studies and case-studies all point to the significant added value of profiles of wind data.

The European Space Agency's (ESA) Aeolus satellite was launched on 22 August 2018 with the first Doppler Wind Lidar (DWL) in space and the first European lidar in space as the payload. The mission's main objective is to provide profiles of high-quality wind component information from the surface up to the lower stratosphere (~30 km, ~10 hPa), using a DWL instrument called ALADIN (Atmospheric LAser Doppler INstrument) in a polar Sun-synchronous, ~320 km altitude dawn–dusk orbit (ESA, 2008). The observations consist of slant path (off-nadir) profiles of the HLOS wind component, pointing in the direction perpendicular to the satellite–Earth surface velocity vector (mostly zonal wind component information). The mission is intended to last at least 3 years. Information about ALADIN can be found in Lux *et al.* (2020a) and Reitebuch (2012).

ECMWF are part of the ESA-funded Aeolus DISC (Data Innovation and Science Cluster) consortium and were part of the team working on the characterization, calibration and validation of the ALADIN instrument and the Aeolus data products (Reitebuch *et al.*, 2020a).

Short-range NWP forecasts have been extensively used to detect observation quality issues, for example: Hollingsworth *et al.*, 1986; Stoffelen, 1999; Lu *et al.*, 2011. This same principle has been applied for Aeolus HLOS winds, via detailed comparisons to the ECMWF short-range forecast (Rennie, 2016), to assess the observation random and systematic errors. We focus on L2B HLOS winds produced in near real time operational processing during the first 2 years of the Aeolus mission, from September 2018 until October 2020. Reprocessed datasets with improved quality and consistency were not yet available for this extensive study. We anticipate further NWP benefits from these in the future.

During the mission so far, the ECMWF monitoring has helped to detect several Aeolus anomalies, and explanations have been found in collaboration within the Aeolus DISC, for example, Weiler *et al.* (2020). Also, the NWP monitoring has supported ESA and industry to perform instrument adjustments, which has led to improvements in the quality of the wind retrievals. One very important issue, which was discovered and resolved in this study, relates to the correlation between systematic HLOS wind errors and ALADIN's telescope primary (M1) mirror temperatures, as discussed in Section 3.4. The correction algorithm by the Aeolus DISC has implemented for this in the ground processing chain.

As part of the mission's calibration and validation (CAL/VAL), Aeolus L2B winds have been compared to various *in situ* observation types, such as radiosondes (Martin *et al.*, 2021), ground-based radar wind profiler (Geiß *et al.*, 2020), ground-based Rayleigh–Mie Doppler lidar (Khaykin *et al.*, 2020) and airborne campaign Doppler lidar data (Lux *et al.*, 2020b; Witschas *et al.*, 2020). Our assessments of wind quality, using the ECMWF short-range forecasts, are complementary to these comparisons against Earth-based *in situ* or remotely sensed winds, benefiting from the high temporal and global coverage of ECMWF's generally accurate wind fields, and with a more similar resolution to Aeolus winds. Our knowledge of the systematic and random errors in ECMWF short-range wind forecasts is sufficient to characterize Aeolus' larger wind errors, in particular when averaged over larger data samples.

The key topic of this article is the assessment of the global NWP forecast impact of Aeolus winds. We used the Observing System Experiment (OSE: Andersson *et al.*, 1991) technique and Forecast Sensitivity Observation Impact (FSOI: Langland and Baker, 2004; Cardinali, 2009) diagnostics in the ECMWF global data assimilation system. OSE results for two different time periods are shown, increasing the confidence in the positive impact found. Aeolus Rayleigh-clear and Mie-cloudy winds were switched on in ECMWF operational data assimilation on 9 January 2020 – a major achievement for a demonstration mission, less than 17 months after launch.

Section 2 describes the methods used to assess the L2B wind quality via NWP monitoring, and the OSE and FSOI impact experiment periods and settings. Section 3 presents the results of the assessment of the quality of L2B winds using the ECMWF short-range forecasts as a reference. Section 4 provides the results of the Aeolus NWP impact

assessment and the remaining sections are the discussion and conclusions.

2 | METHODS

2.1 | Aeolus Level-2B data

Aeolus L2B wind products are the output of a multiple-stage ground-processing chain, that has been developed since the early 2000's. A description of the processing levels from raw data to L1B (Reitebuch *et al.*, 2018) and up to L2B is given in ESA (2008). Tan *et al.* (2008) explains the original concept of the L2B processor (wind retrieval), but the L2B Algorithm Theoretical Basis Document (ATBD) provides an up-to-date description of the latest scientific algorithms and the input/output of the processor (Rennie *et al.*, 2020). The key observational output from the L2B processor is the HLOS wind, which is suitable for use in NWP and scientific research, due to several important extra processing steps relative to the Level-1B (L1B) HLOS wind products. The most important is accounting for the slight influence of atmospheric temperature and pressure (Dabas *et al.*, 2008) on the Rayleigh-clear winds. The L2B processor also performs classification of measurement-scale (∼3 km; highest-resolution data, which is downlinked from the satellite) data into clear and cloudy conditions and performs flexible horizontal averaging of measurement-scale signal data to the observation scale (typically up to 87 km for Rayleigh-clear winds). It also accounts for Mie backscatter in the Rayleigh-clear winds and provides a realistic random instrument error estimate with each wind result.

The L2B winds come in four types due to the atmospheric classification into clear-air or cloudy-air conditions: Rayleigh-clear, Rayleigh-cloudy, Mie-clear and Mie-cloudy. We focus on the Rayleigh-clear and Mie-cloudy winds, since they are better quality. A typical example of Aeolus L2B HLOS winds on 1 September 2020 is shown in Figure 1a for Rayleigh-clear and Figure 1b for Mie-cloudy. Being an active space-borne optical instrument, ALADIN is attenuated by optically thick ice and water cloud, aerosols or the ground, hence areas exist closer to the surface with no wind measurements (shaded grey). The Mie-cloudy winds primarily come from optically thick cloud tops, from within optically thin clouds and to a lesser extent from aerosols. Mie-cloudy winds have poorer spatial coverage than the Rayleigh-clear winds which are based on molecular returns.

ALADIN's line-of-sight points perpendicularly to the satellite–Earth relative velocity with an angle of ∼10° from the zonal direction (outside of polar regions). Therefore, the HLOS winds provide information mostly on the zonal rather than the meridional wind component. However, near the Poles the meridional wind component information dominates. Away from the Poles, for ascending orbit phase, Aeolus measures the predominantly westerly jet streams as positive HLOS winds, and for descending orbit phase the westerly jet streams are measured as negative HLOS winds. This is seen for the Rayleigh-clear winds in Figure 1.

The data are accumulated in vertical bins with a thickness varying from 0.25 to 2 km, defined by the range-bin settings (RBS). Aeolus allows variable RBS along the orbit, as seen for the Rayleigh-clear in Figure 1a. The RBS have been refined during the mission to try to achieve the best NWP impact and scientific benefit from the 24 available range-bins, for example, by using a higher top altitude over the Poles to capture the polar vortex (and potential Mie-cloudy winds from polar stratospheric clouds). A higher top altitude results in poorer vertical resolution at lower levels. Improved vertical resolution in the extratropical polar-front jet stream and in the tropical upper troposphere was chosen, due to increased vertical wind shear in those regions which is of importance for NWP.

The Rayleigh-clear wind random error depends on many factors. Shot-noise from the detection process of signal photons dominates, so with an atmospheric path useful signal magnitude (S), the Rayleigh-clear wind random error is proportional to $S^{-1/2}$ (not considering solar background noise). Atmospheric path signal depends on:

- The output laser pulse energy and the optical efficiency of the transmit-and-receive path of the instrument. These have varied considerably during the mission.
- Satellite-to-target distance (range). The atmospheric signal received is inversely proportional to the square of the distance. The average range varies from a minimum at the Equator of ∼376 km to a maximum of ∼420 km at the South Pole, and ∼393 km at the North Pole.
- The amount of signal accumulation. This depends linearly on the vertical thickness of the range-bin and on the horizontal accumulation length.

Another important factor for the Rayleigh-clear wind random error is the level of solar background noise in the ultraviolet (UV) operating wavelength of the instrument, which varies along the orbit and by season according to the solar illumination at the target. It is largest when passing over the summer pole.

Mie-cloudy winds have higher precision than Rayleigh-clear due to backscatter from clouds being typically an order of magnitude stronger than from clear air, and the lack of Doppler broadening for the Mie

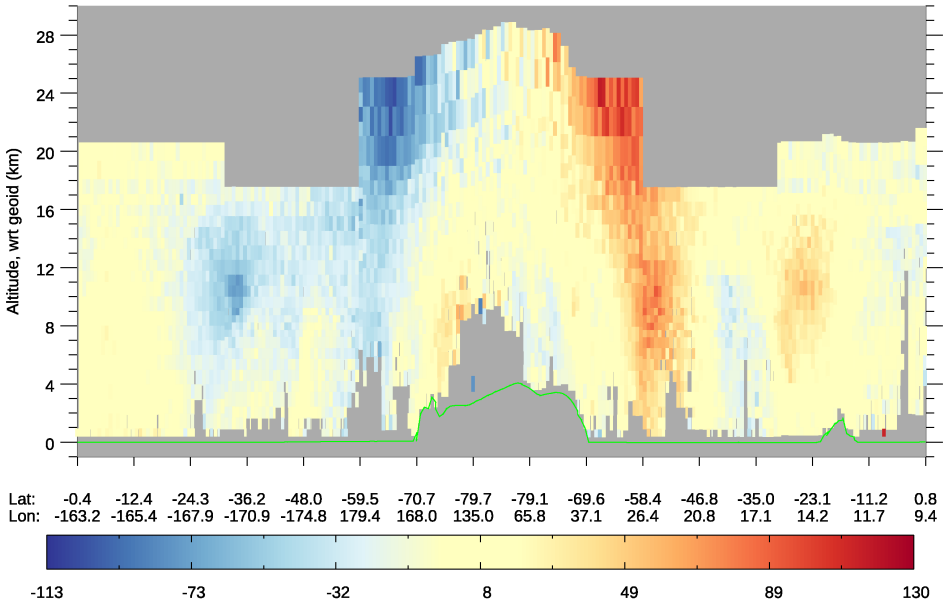

(a) L2B Rayleigh-clear HLOS winds

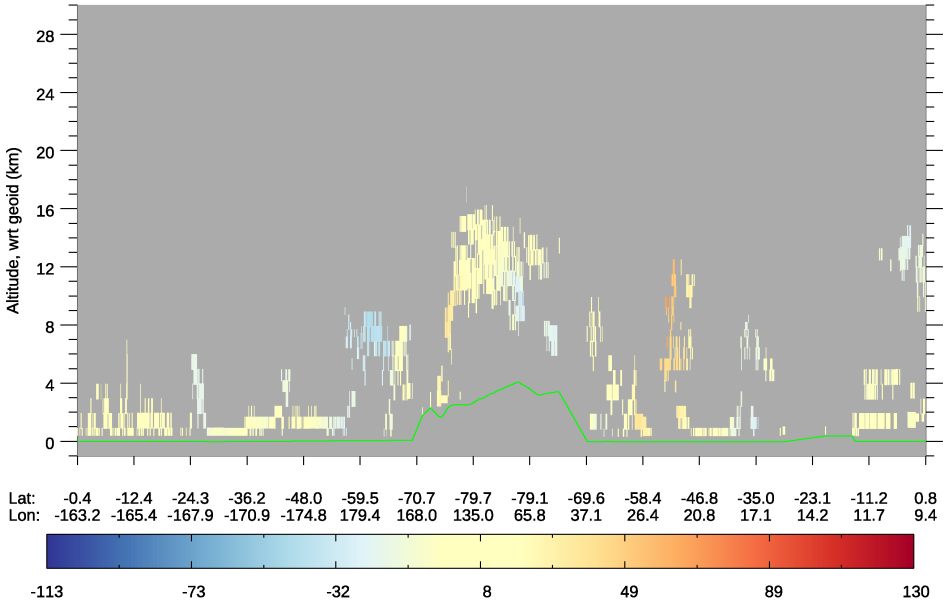

(b) L2B Mie-cloudy HLOS winds

FIGURE 1 L2B (a) Rayleigh-clear and (b) Mie-cloudy HLOS wind retrievals ($m \cdot s^{-1}$) for half of an orbit on 1 September 2020 (orbit number 11747); starting in the descending orbit phase near the Equator. The vertical axis is the geometric height relative to EGM96 (Earth gravity model from 1996) geoid and the horizontal axis is the time along the orbit (but labelled with latitude and longitude geolocation along the orbit). Winds blowing away from the satellite produce positive HLOS winds and blowing towards produce negative HLOS winds. Grey areas indicate an absence of winds. Each observation is plotted as a coloured rectangle with a boundary indicating the spatial limits and hence resolution of the observation. The digital elevation model used in the wind retrieval is shown in green. Antarctica is clearly visible as high ground (>3 km) at the lowest latitudes, near the centre

backscatter compared to the broad spectral bandwidth Rayleigh–Brillouin spectrum (Witschas *et al.*, 2012). Mie-cloudy winds from weak backscatter such as from typical aerosol layers are sensitive to the signal levels though.

L2B processor settings used since March 2019 result in Mie-cloudy winds of horizonal resolution up to ~12 km (previously up to ~87 km), compared to the Rayleigh-clear (~87 km). The shot-noise-dominated Rayleigh measurements mean longer horizontal averaging is necessary to achieve acceptable random errors for Rayleigh-clear winds. Despite the higher resolution of the Mie-cloudy winds, the Rayleigh-clear winds are ~1.7 times noisier than the Mie-cloudy (in standard deviation) (see Section 3.2).

The L2B data investigated in this article is sourced from the near real-time (NRT) operationally produced products by ESA's Payload Data Ground Segment (PDGS). The ground segment processing algorithms, instrument performance and data availability has varied considerably during the mission, leading to some natural boundaries for NWP impact assessment time periods. Rennie and Isaksen (2020) provides a description of some of these changes in the NRT L2B data properties until May 2020, such as the characteristics from the mission's commissioning phase (from September 2018 to January 2019). A major change

was the switch from the first flight model laser (FM-A) to the second one (FM-B) in June 2019; see Lux *et al.* (2020a).

An important component to the random error evolution of both Rayleigh-clear and Mie-cloudy winds is the improvement of the data processing algorithms during the mission and changes in applied calibration data (for which the quality can vary), for example, see Rennie and Isaksen (2020).

2.2 | Observation minus background departure statistics

A state-of-the-art data assimilation system and forecast model (such as ECMWF's) is a powerful tool for monitoring and evaluating a new observing system. The forward modelled observation equivalent (B) (also known as background) can be compared to the observation (O). O–B departure (or innovation) statistics provide valuable information on the quality of the observations.

Assuming $O = T + \epsilon_O$ and $B = T + \epsilon_B$, where T is the true HLOS wind, ϵ_O is the observation error and ϵ_B is the background error, then variance and expectation of innovation statistics can, with some assumptions, be estimated as:

$$Var(O-B) = Var(\epsilon_O) + Var(\epsilon_B) - 2Cov(\epsilon_O, \epsilon_B),$$

$$E(O-B) = E(\epsilon_O) - E(\epsilon_B).$$

The observation random error estimate (standard deviation, σ) is as follows (assuming the covariance of observation and background errors is negligible).

$$\sigma(\epsilon_O) = \sqrt{Var(\epsilon_O)} \approx \sqrt{Var(O-B) - Var(\epsilon_B)}.$$

The observation systematic error (bias) estimate is as follows (assuming that the expectation of background error is relatively small compared to the observation bias).

$$E(\epsilon_O) = E(O-B) + E(\epsilon_B) \approx E(O-B).$$

This observation random error estimate requires knowledge of the background error variance, $Var(\epsilon_B) = \sigma^2(\epsilon_B)$. The ECMWF background is of course not the truth, but averaged over large spatial- and time-scales it has a high level of accuracy and good precision.

Estimates for $\sigma(\epsilon_B)$ were derived using "Desroziers diagnostics" (Desroziers *et al.*, 2005) using radiosonde zonal wind and Aeolus HLOS wind departures. This led to a typical range for $\sigma(\epsilon_B)$ of 1.5 to 2.5 $\mathrm{m{\cdot}s^{-1}}$ in HLOS wind space, varying with atmospheric pressure (altitude) and geolocation (smaller errors near the surface). Due to the variability of $\sigma(\epsilon_B)$, we have used this range to define confidence intervals for our $\sigma(\epsilon_O)$ estimates.

HLOS wind space $\sigma(\epsilon_B)$ is available via the Ensemble of Data Assimilations spread (EDA: Isaksen *et al.*, 2010) available with each observation. This gave a mean $\sigma(\epsilon_B)$ of $\sim$1 $\mathrm{m{\cdot}s^{-1}}$ at Rayleigh-clear and $\sim$1.2 $\mathrm{m{\cdot}s^{-1}}$ at Mie-cloudy geolocations. This is unrealistically small compared to the departure-based metrics. The lack of variance is due to: spectral truncation, the values apply at the start of the four-dimensional variation (4D-Var) window and overall imperfect scaling of assigned observation errors in the ECMWF analysis. However, the EDA derived $\sigma(\epsilon_B)$ has realistic geographical gradients (such as being larger in the tropical upper troposphere) even if the absolute values are too small.

We found the maximum global average bias, varying with altitude, of radiosondes zonal and meridional wind component, $E(O-B)$, to be approximately 0.3 $\mathrm{m{\cdot}s^{-1}}$ (in several periods), therefore we assume this represents the maximum possible global average background forecast bias over large samples. Martin *et al.* (2021) showed a good agreement between Aeolus L2B departures with respect to two NWP backgrounds (DWD and ECMWF) and collocated radiosondes, which gives confidence that the large spatial- and time-scale ECMWF model winds are a trustworthy reference for inferring Aeolus biases.

ECMWF's Integrated Forecasting System (IFS) HLOS wind observation operator (used to calculate B) is:

$$H(u,v) = -u\sin\varphi - v\cos\varphi.$$

The HLOS wind is a linear function of the model zonal wind component (u) and meridional wind component (v) which are interpolated to the observation geolocation point (latitude, longitude and geometric height). φ is the azimuth angle, describing the line-of-sight pointing of the laser projected onto the horizontal plane; it is provided as part of the observation geolocation information. The horizontal and vertical interpolation of the model wind field to the observation geolocation uses standard IFS methods applied for *in situ* observations (ECMWF, 2020). Further details on this observation operator can be found in Rennie and Isaksen (2020).

The point observation operator is a reasonable approximation in the horizontal dimension given that the effective resolution of ECMWF's global model is similar to the horizontal resolution of Rayleigh-clear winds (on the order of 4–8 times the model grid spacing (Abdalla *et al.*, 2013) or even larger (Stoffelen *et al.*, 2020b)). The ECMWF operational deterministic model configuration is used to provide the departures. It has a horizontal resolution $\mathrm{T_{CO}}$ (triangular– cubic-octahedral) 1,279 (Malardel *et al.*, 2016) ($\sim$9 km grid spacing at midlatitudes) and 137 vertical levels

up to ~80 km. The Mie-cloudy winds have higher horizontal resolution (~12 km) than the effective ECMWF model resolution, which means representativeness errors should be considered in their assimilation (see Section 2.3); effectively we inflate the assigned observation error.

The point observation operator is less appropriate in the vertical dimension, given that the model's winds can vary significantly over Aeolus' thickest (1–2 km) range-bins. In the tropical upper troposphere, and along tropospheric frontal zones, the model HLOS wind vertical shear is often more than 20 $m \cdot s^{-1}$ per km (not shown). This is despite the model underestimating vertical wind shear (Houchi *et al.*, 2010). Also, particularly for the cloud backscattered Mie-cloudy winds (Sun *et al.*, 2014), it is unknown where the cloud lies within an Aeolus range-bin. However, the wind is assigned to the centre of the range-bin, and this discrepancy introduces a forward model representativeness error. For Rayleigh-clear winds an attenuated backscatter vertical weighting function could be used in the observation operator.

Departure statistics were calculated by ingesting the HLOS wind retrievals and associated meta-data, via the WMO L2B BUFR (Binary Universal Form for the Representation of meteorological data) format, into the ECMWF 4D-Var analysis with a 12 hr assimilation window ("delayed cut-off": Haseler, 2004) and hence calculating the departure statistics. When available, we have used ECMWF operationally produced departures in our investigations, but prior to December 2018 an offline analysis at the operational resolution was used. Time-series of departure statistics for different pressure ranges and partitioned into different orbit phases are provided in Section 3.1.

Since 9 January 2020, Aeolus L2B winds have been operationally assimilated at ECMWF, implying that the background departures are no longer independent of past Aeolus winds; it is unclear if this affected the Aeolus error estimates but there is no obvious discontinuity in the time series, so it probably did not.

2.3 | Observing system experiments

The OSEs performed focused on the assessment of Aeolus L2B HLOS winds during time periods where an appropriate bias correction for the L2B winds was available (whether via the L2B processing or through ECMWF's own bias correction methods as part of the data assimilation system), and when the operational ground processing algorithms had reached a sufficient level of maturity. See Table 1 for details of the two OSE periods tested and of the Aeolus L2B data used.

The early FM-B laser period L2B dataset was obtained from the operationally produced data. The test period started on 2 August 2019, because before that inappropriate calibration files were applied. A discussion of the type of bias corrections that were applied to the L2B data for both OSE periods is provided in Section 3.4.

Both OSEs used the same assigned HLOS wind observation error modelling, which is:

$$\sigma(\epsilon_{O,\text{assign}}) = \sqrt{\alpha^2\sigma^2(\epsilon_{O,\text{instr}}) + \sigma^2(\epsilon_{O,\text{rep}})},$$

where $\sigma(\epsilon_{O,\text{rep}})$ is the representativeness error standard deviation, $\sigma(\epsilon_{O,\text{instr}})$ is the L2B processor reported instrument error standard deviation (provided with each wind result) and α is the scaling factor applied for the generally underestimated instrument error estimate. The L2B processor estimated error (an instrument noise estimate via propagation of errors from the detector counts) correlates very well with the standard deviation of O–B departures and is thought to be realistic, particularly so for the Rayleigh-clear winds. The observation error parameters were determined via a combination of "Desroziers diagnostics" and trial and error in OSEs. They are listed in Table 2.

Some data selection and quality control (QC) was applied to the L2B data in both OSE periods. Only Rayleigh-clear and Mie-cloudy winds with "valid" overall L2B confidence flag were used. Rayleigh-cloudy or Mie-clear winds were not assimilated. All data within 20 hPa (~160 m) of the surface were discarded to avoid using spurious ground returns. Rayleigh-clear winds below 850 hPa were discarded to avoid some apparent degradation from the generally noisy wind results due to thin range-bins and atmospheric attenuation in the atmospheric boundary layer.

Data with large L2B estimated instrument standard error were discarded since it was found to help eliminate gross errors, particularly for the Mie-cloudy. The thresholds, before error scaling, were 12 $m \cdot s^{-1}$ for Rayleigh-clear winds above 200 hPa and 8.5 $m \cdot s^{-1}$ for Rayleigh-clear winds below 200 hPa. For Mie-cloudy winds the threshold was 5 $m \cdot s^{-1}$ at all altitudes. Rayleigh-clear data with horizontal accumulation lengths below 60 km were discarded to avoid spurious clear-air returns.

Aeolus impact assessment during the early mission (commissioning phase) and in the late FM-A laser period, during which the NRT processing had many issues and hence does not give a fair representation of Aeolus data quality, is provided in Rennie and Isaksen (2020). We present OSEs from the FM-B laser period. The OSEs use the full observing system nominally assimilated at ECMWF that is, operational data exclusion lists, so the Aeolus impact is representative of what would be produced in an operational NWP environment.

TABLE 1 OSE periods investigated, processing chain information and applied L2B data

OSE period name	Start	End	L1Bp version	L2B data source	L2Bp version	PDGS baseline	Data assimilation system	Bias correction method	Comments
Early FM-B	2 August 2019	31 December 2019	7.06, then 7.07 since 31 October 2019	PDGS NRT dataset	3.11, then 3.2 since 31 October 2019	2B06 then 2B07 since 31 October 2019	CY46R1.2 4D-Var outer loop resolution: $T_{CO}99$ (~29 km grid) Control ID: Hbnq Experiment ID: Hdai (Rayleigh and Mie); Hcvk (Mie only)	*E*(O-B) look-up table method (see Section 3.4 for details)	See Section 3.1 for variation in observation quality and range-bin settings.
Mid-2020 FM-B	4 April 2020	20 September 2020	7.08	Offline L2B processed dataset at ECMWF until 19 April, then PDGS NRT dataset since 20 April	3.3	2B10	CY47R1.1 4D-Var outer loop resolution: $T_{CO}399$ (~29 km grid) Control ID: hel1 Experiment ID: hel4	M1-temperature bias corrected L2B data (see Section 3.4 for details)	See Section 3.1 for variation in observation quality and range-bin settings. 10 days data excluded due to ALADIN testing periods.

TABLE 2 Parameters used in the assigned data assimilation observation error

Wind type	L2B processor instrument error estimate scaling factor α	Representativeness error ($m \cdot s^{-1}$) $\sigma(\epsilon_{O,rep})$
Rayleigh-clear	1.4	0
Mie-cloudy	1.25	2

2.4 | Forecast sensitivity to observation impact set-up

FSOI is a cost-effective method used by many NWP centres, typically to evaluate 24 hr forecast impact from observations. FSOI measures the impact of observations in the context of all the other observations assimilated (Langland and Baker, 2004). The ECMWF FSOI is using a global dry energy norm error. It relies on the accuracy of the model's adjoint and is therefore limited to short-range forecasts assessment. The FSOI short-range impact does not guarantee similar levels of impact on the medium-range forecasts, so OSEs are still required for a proper evaluation. The FSOI metric can be summed up over time and space and into different components of the observing system to get the relative impact. Aeolus FSOI is available since the operational assimilation started on 9 January 2020.

3 | ASSESSMENT OF HLOS WIND RETRIEVAL ERROR STATISTICS

The error properties of Aeolus L2B HLOS wind retrievals are assessed via O–B departures using the methods explained in Section 2.2.

3.1 | Time-series of HLOS wind error statistics

Global daily time-series of the L2B Rayleigh-clear HLOS wind error properties during the mission from 7 September 2018 to 5 October 2020 are shown in Figure 2. The statistics are split into pressure ranges: 100–800 hPa (~2–16 km) to approximately represent the free troposphere and above 100 hPa to represent the lower stratosphere, and then further split into ascending and descending orbit phase. There are some gaps in the time series due to the exclusion of data during known instrument anomalies and tests for which the quality of the winds was affected and gaps due to ALADIN not operating. A background QC threshold was applied to mitigate the effect of outliers, by rejecting data where the absolute O–B departure exceeds 15 $m \cdot s^{-1}$, which is roughly a 3-σ check. The HLOS wind random error statistic is strongly influenced by the mean range-bin thickness, hence this is also shown in Figure 2.

Global daily time-series of the L2B Mie-cloudy HLOS wind error statistics during the mission are shown in Figure 3. The statistics are split into pressure ranges: 800–1,100 hPa (surface to about 2 km) to roughly represent the planetary boundary layer (PBL) and 100–800 hPa (~2–16 km) roughly representing the free troposphere, and then further split into ascending and descending orbit phase. The Mie-cloudy time-series used a background QC threshold of 10 $m \cdot s^{-1}$, which is roughly a 3-σ check for Mie-cloudy winds. Mie-cloudy winds are relatively scarce in the stratosphere and therefore not shown.

3.2 | Assessment of HLOS wind random error statistics

The Rayleigh-clear random error increased during the FM-A laser period (from mission start to mid-June 2019), with the rate of degradation increasing with time; this is evident in the troposphere and the lower stratosphere, as seen on Figure 2. This was due to: an increasing percentage of uncorrected "hot pixels" (Weiler *et al.*, 2020); a downward trend in atmospheric signal levels due to decreasing output laser energy (Lux *et al.*, 2020a; Reitebuch *et al.*, 2020a); and seasonal changes in the M1-mirror-temperature dependent bias variations (which are largest at Northern Hemisphere summer solstice; see Section 3.4), which manifests as increased random error in daily average statistics.

For the early FM-B laser period in August 2019, the estimated Rayleigh-clear random error was significantly smaller than compared to late FM-A data, but similar in the free troposphere to the early FM-A data (September 2018) (despite the assigned range-bins being thinner for early FM-B compared to early FM-A). The FM-B random errors then generally increased due to decreasing atmospheric path signal (Reitebuch *et al.*, 2020b) and thinner range-bin settings. The random error for FM-B was approximately 1 $m \cdot s^{-1}$ larger in August 2020 compared to August 2019 in the free troposphere.

The Mie-cloudy random errors are larger for early FM-B than for the early FM-A period. This is not yet understood, but may be due to a combination of factors such as: poorer quality Mie calibration data; shorter average horizontal accumulations (~50 km in early FM-A, ~12 km in FM-B, therefore less accumulated signal); modified L2B processor classification algorithm settings; and changes in vertical range-bin settings. Decreasing the horizontal averaging length of the Mie-cloudy winds from typically 50 to 12 km on 5 March 2019 gave a factor 2–3 increase in the

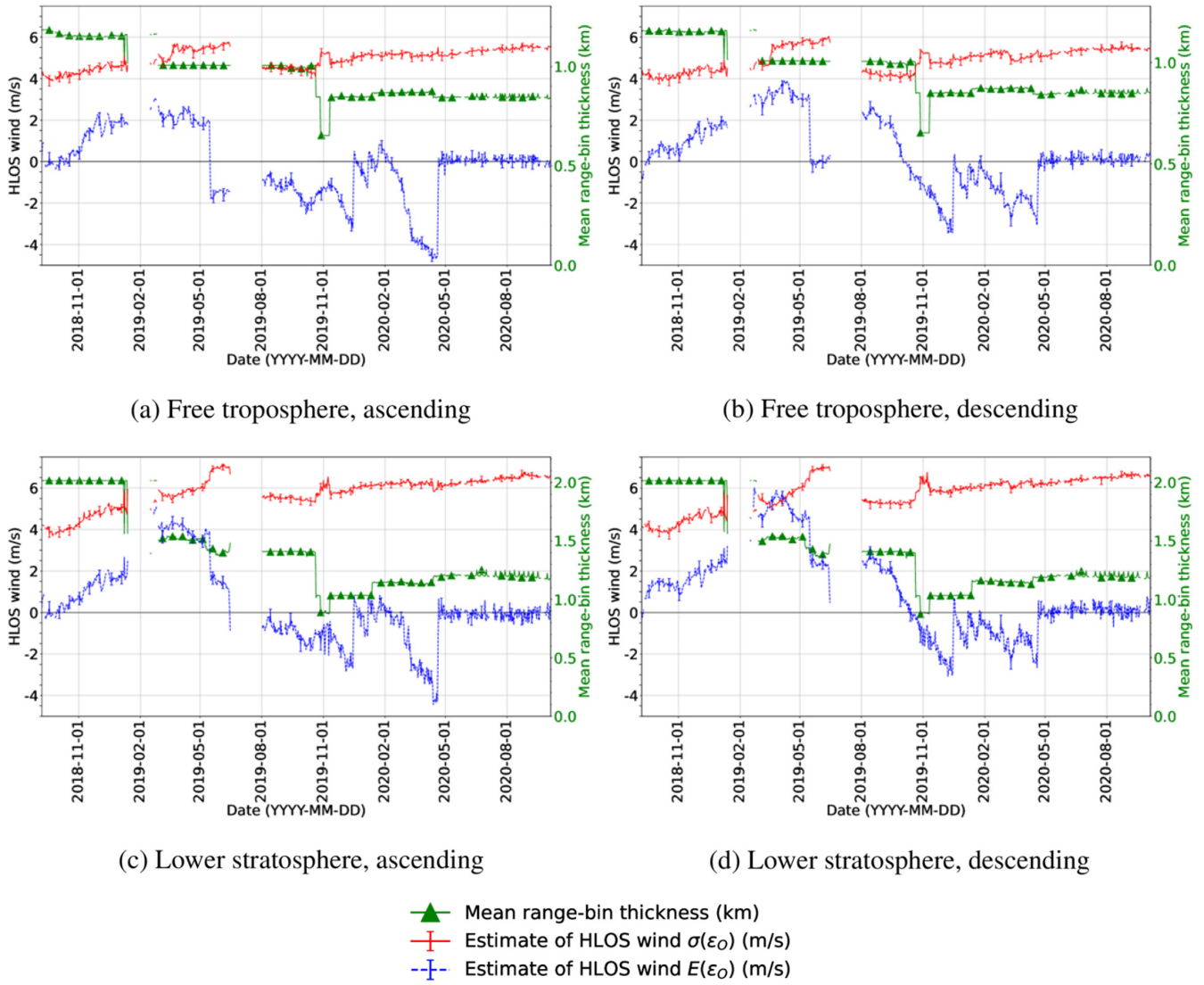

FIGURE 2 Time series from 7 September 2018 until 5 October 2020 of L2B Rayleigh-clear HLOS wind estimated bias ($E(\epsilon_O)$) and estimated random error ($\sigma(\epsilon_O)$). Statistics for the troposphere (100–800 hPa) are shown in the top row for (a) ascending orbit phase and (b) descending orbit phase. Statistics for the lower stratosphere (above 100 hPa) are shown in the bottom row for (c) ascending orbit phase and (d) descending orbit phase. Each datum corresponds to a global sample from 1 day. Also shown is the mean range-bin thickness of the wind retrievals. The error bars represent the error estimate uncertainty as explained in Section 2.2

number of winds and only led to a small increase (~5%) in standard deviation of O–B, which is because the cloud backscatter is sufficiently strong to not be a limiting factor in the wind errors (this agrees with pre-launch predictions in Šavli *et al.* (2019)). Figure 3 shows an increase in random error occurred on 16 May 2020 associated with a processing baseline update involving the application of a new Mie calibration file to decrease systematic errors.

Tables 3 and 4 summarise the estimated global average random observation error, $\sigma(\epsilon_O)$, for Aeolus L2B HLOS winds throughout the mission up to October 2020 for the defined pressure ranges. The tables are partitioned into time periods to reflect the variations during the mission. The Mie-cloudy winds are significantly less noisy than the Rayleigh-clear, with the best case 2.8 $m \cdot s^{-1}$ random error (1-σ), whereas the best performance for the Rayleigh-clear is 4 $m \cdot s^{-1}$, peaking at about 9 km altitude.

3.3 | Assessment of HLOS wind systematic error statistics

Large time-varying biases for Rayleigh-clear and Mie-cloudy winds are evident in Figures 2 and 3, as well as differences between ascending and descending orbit

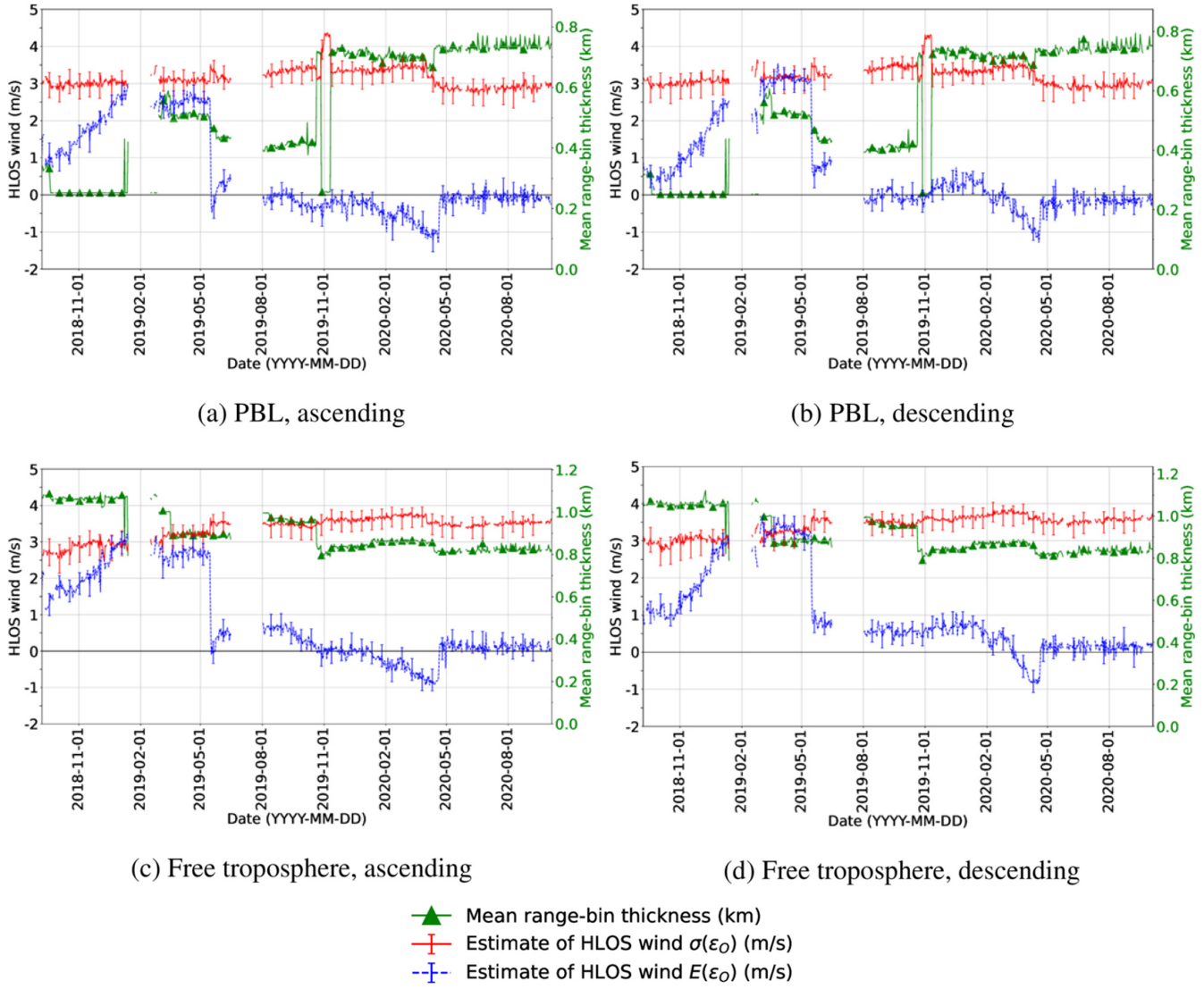

FIGURE 3 Similar to Figure 2, but for L2B Mie-cloudy HLOS winds statistics for the planetary boundary layer (PBL, 800–1,100 hPa) are shown in the top row for (a) ascending orbit phase and (b) descending orbit phase. Statistics for the free troposphere (100–800 hPa) are shown in the bottom row for (c) ascending orbit phase and (d) descending orbit phase

TABLE 3 A summary of the estimated global average random error ($\sigma(\epsilon_O)$) for Aeolus L2B Rayleigh-clear HLOS winds split by atmospheric layer

Pressure range	Time period for each laser	One-σ observation error estimate (m·s^{-1})	
		FM-A	FM-B
Free troposphere	Early	4.0	4.5
Free troposphere	Late	6.0	5.5
Lower stratosphere	Early	4.0	4.0
Lower stratosphere	Late	7.0	6.5

TABLE 4 A summary of the estimated global average random error ($\sigma(\epsilon_O)$) for Aeolus L2B Mie-cloudy HLOS winds split by atmospheric layer (PBL is planetary boundary layer)

Pressure range	Time period for each laser	One-σ observation error estimate (m·s^{-1})	
		FM-A	FM-B
Free troposphere	Early	2.8	3.5
Free troposphere	Late	3.5	3.5
PBL	Early	3.0	3.5
PBL	Late	3.0	3.6

phases, particularly for the Rayleigh-clear winds. An explanation for the latter is given in Section 3.4.

During the FM-A period, the L2B Rayleigh-clear global average bias had a positive trend (of around 0.4 m·s^{-1} per month) which settled in March 2019. A new calibration file was implemented on 16 May 2019, reducing the positive bias (but still ascending/descending differences). The bias then remained steady until laser FM-A's switch-off in

mid-June 2019. When the first reasonable FM-B calibration file was applied from 2 August 2019 the wind bias was close to zero for ascending orbits, but positively biased by 2 m·s^{-1} for descending orbits. However, it then drifted to negative values (at a faster rate for descending orbits), particularly from mid-September 2019. The drift rate varied with time from around −0.9 m·s^{-1} per month from August to December 2019 to −1.3 m·s^{-1} per month from January to April 2020 (average combining ascending and descending). The bias reduction steps on 16 December 2019 and 7 January 2020 were due to the application of manual bias correction which is an option in the L2B processing settings.

Aeolus DISC investigations, for example Reitebuch *et al.* (2020b), found that the negative bias drift for FM-B was due to a drift in the internal path Rayleigh response, which is not replicated in the corresponding atmospheric path Rayleigh response, combined with using fixed calibration files. The drift in internal Rayleigh spectrometer response is thought to be due to changes in pointing (angle of incidence) of the laser light upon the spectrometers, rather than a change in laser frequency. Decreases in internal and atmospheric signal levels with time throughout FM-B are probably linked to the internal path drift (likely to be a geometrical clipping of signal through an aperture (Reitebuch *et al.*, 2020b)).

The improvement in bias since 20 April 2020 – close to zero and steady with time – is the result of the operational implementation of the M1-mirror-temperature dependent bias correction scheme (see Section 3.4), which also in effect corrects the internal path Rayleigh response drift induced offset bias.

The Mie-cloudy global average bias had a positive trend for FM-A, although it settled in April 2019. The bias improved by 2.0–2.5 m·s^{-1} when a new calibration file was applied in May 2019. The bias for FM-B data was reasonably stable and less than 1 m·s^{-1} until January 2020, after which it gradually became more negative (this has not yet been explained). As with the Rayleigh-clear, the bias stabilised significantly after the M1-mirror-temperature dependent bias correction went operational on 20 April 2020.

3.4 | An explanation for the systematic error variations with orbital phase – M1-mirror-temperature dependence

Throughout the mission Aeolus O−B departures showed the presence of large magnitude biases (several m·s^{-1} HLOS) differing between ascending and descending orbit phases (as is evident in Figures 2 and 3); particularly for the Rayleigh-clear winds. The biases were confirmed with respect to radiosondes and another NWP assimilation system (Martin *et al.*, 2021), so we can be confident that Aeolus is the source of the bias.

The Rayleigh-clear bias varies with geolocation as is shown in Figure 4. Here $E(O-B)$ is binned by the orbit phase angle (argument of latitude) and by longitude from week-long samples (the bias remains roughly the same in geographical pattern over a week time-scale). Argument of latitude is defined as 0° at the ascending node Equator crossing and 360° when back ascending at the Equator. The Rayleigh-clear bias can change significantly over a monthly time-scale for example, a decrease of 3 m·s^{-1} during April 2019 at the North Pole (argument of latitude of 90° in Figure 4a,b). In August 2019 it varied considerably with argument of latitude and longitude (Figure 4c); the range of bias variation is greatest in NH summer, that is, a range of 10 m·s^{-1} in August compared to 5 m·s^{-1} in April and December 2019. There is also an orbit phase dependence to the Mie-cloudy bias (Figure 5), but the bias range of ∼2.5 m·s^{-1} is much smaller than for the Rayleigh-clear. Also, the longitudinal dependence was very small for the Mie-cloudy.

Inspired by research (Bell *et al.*, 2008) that resolved Special Sensor Microwave Imager/Sounder (SSMIS) bias issues, we correlated Aeolus biases, on a sub-orbital time-scale, with the available satellite housekeeping data, to try to determine the cause of the bias. It became clear that there was a link between the ALADIN telescope primary (M1) mirror (Korhonen *et al.*, 2008) temperatures and the Rayleigh-clear bias from maps of bias compared to mean M1 temperature in the Northern Hemispheric summer over several days, but the relationship had complicated nonlinear characteristics. The M1 temperature readings are provided by thermistors which are distributed across the mirror; many of which provide readings every 4 seconds. An example of a selection of the temperature readings during 8 hr on 8 August 2019 is shown in Figure 6. There is an orbital periodicity (∼1.5 hr) to the temperature readings, but never exactly repeated. Investigations by the Aeolus DISC and ESA confirmed that the M1 mirror temperatures vary along the orbit in response to varying top of atmosphere radiation (short- and long-wave) and the M1 mirror's onboard thermal control mechanism in response to this, hence the periodicity along the orbit.

A strong linear correlation between the gradients (differences) of temperature across the mirror and the bias $E(O-B)$ was discovered. The difference of the mean of the mirror's outer edge temperatures minus the mean of the near-centre temperatures showed a particularly high correlation of 93% on 8 August 2019, see Figure 7. $E(O-B)$ is derived from a 2 min (∼860 km along-track) sample, taken

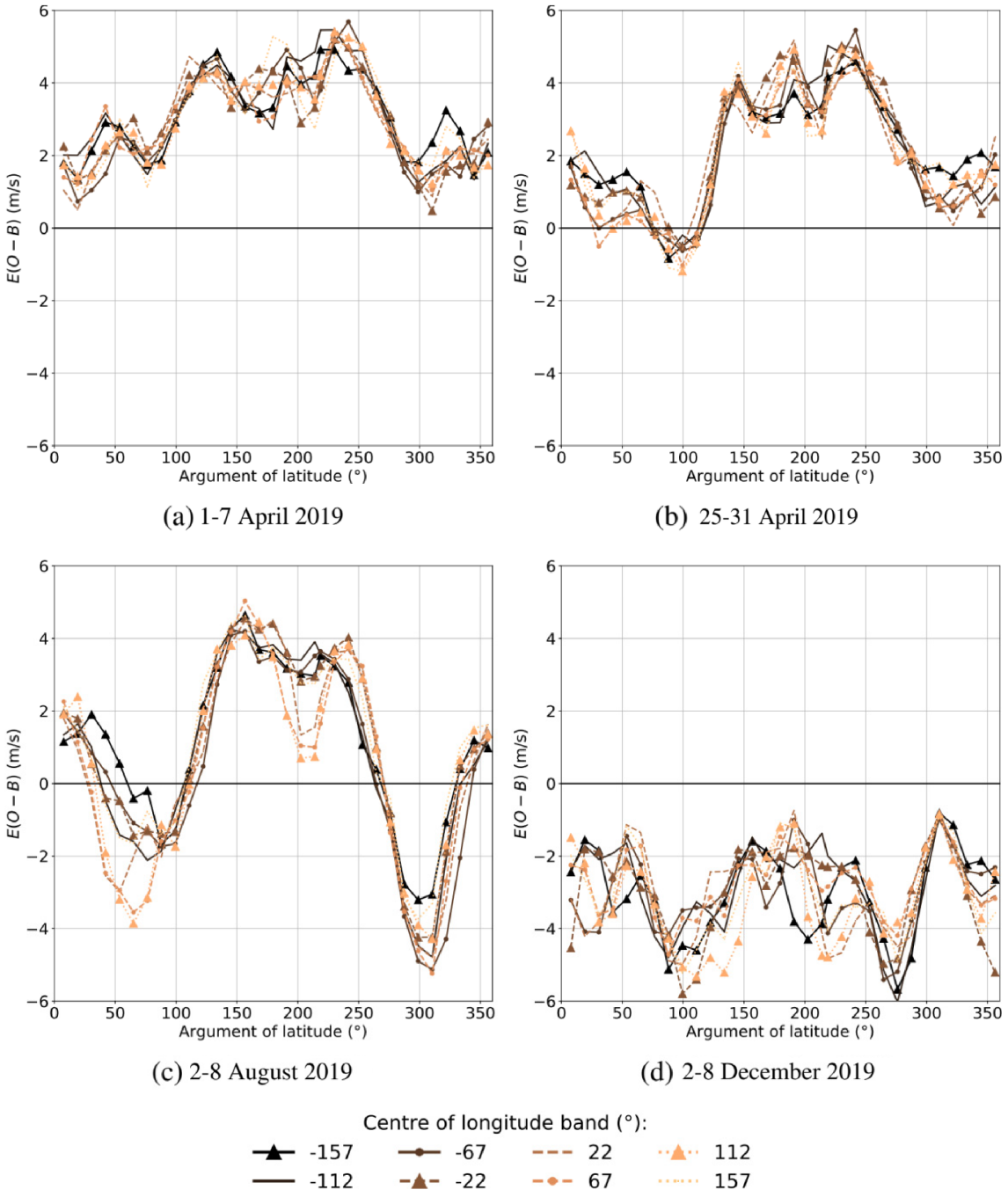

FIGURE 4 Rayleigh-clear bias ($E(O-B)$) binned by argument of latitude (orbit phase angle) and longitude for (a) 1–7 April 2019, (b) 25–31 April 2019, (c) 2–8 August 2019 and (d) 2–8 December 2019. There are 32 argument of latitude bins (11.25° wide) and eight longitude bins (45° wide). The argument of latitude and longitude bins are referenced by the value at the centre of the bin. For visualisation purposes eight longitude bins are shown, however in practical bias correction for the early FM-B OSE, 10 bins was found to work best

over all altitudes. Such a sample is typically made up of 200 winds (assuming 20 available vertical range-bins and 10 profiles). The Rayleigh-clear HLOS wind bias is very sensitive to the magnitude of the mirror temperature gradient for example, 47 $m \cdot s^{-1}$ per Kelvin on 8 August 2019.

A bias correction was developed using the M1 temperature readings (available in NRT) as predictors, and the linear regression coefficients trained from past data. The M1-temperature-dependent bias correction works well, as is shown in Figure 8 for 9 August 2019; for which the M1-temperature bias correction linear regression coefficients were derived from independent data the day before (8 August 2019, as shown in Figure 7). The 24 hr sample standard deviation of the $E(O-B)$ is reduced from

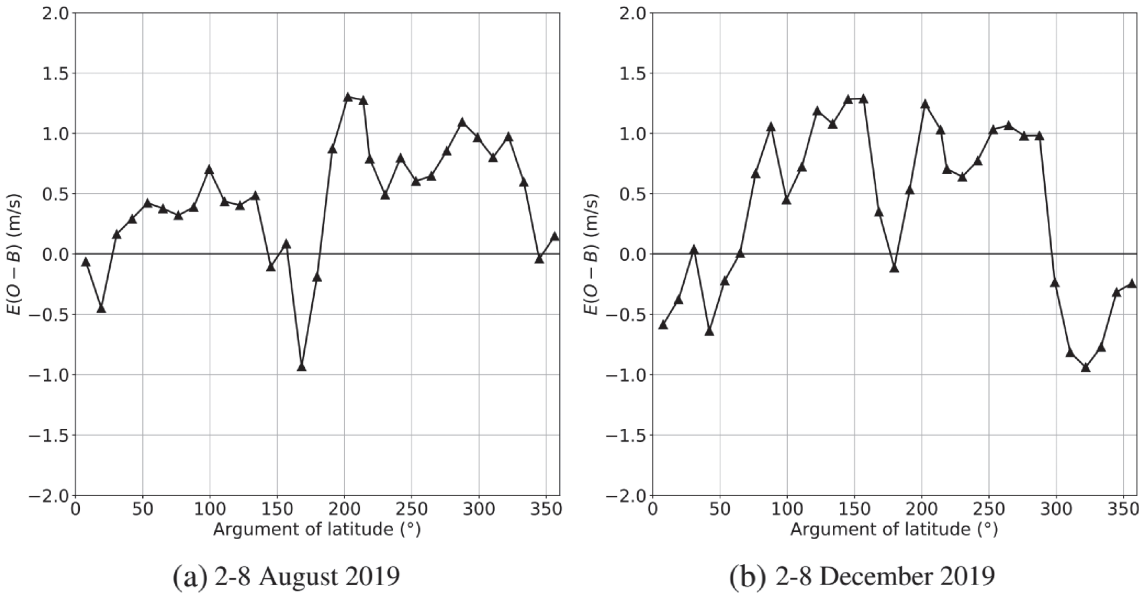

FIGURE 5 Mie-cloudy bias ($E(O-B)$) binned by argument of latitude (orbit phase angle) for (a) 2–8 August 2019 and (b) 2–8 December 2019. There are 32 argument of latitude bins (11.25° wide)

FIGURE 6 A selection of M1 mirror temperature readings from 0400 to 1200 UTC on 8 August 2019. The labels for the different thermistors are given, which identify them within ALADIN

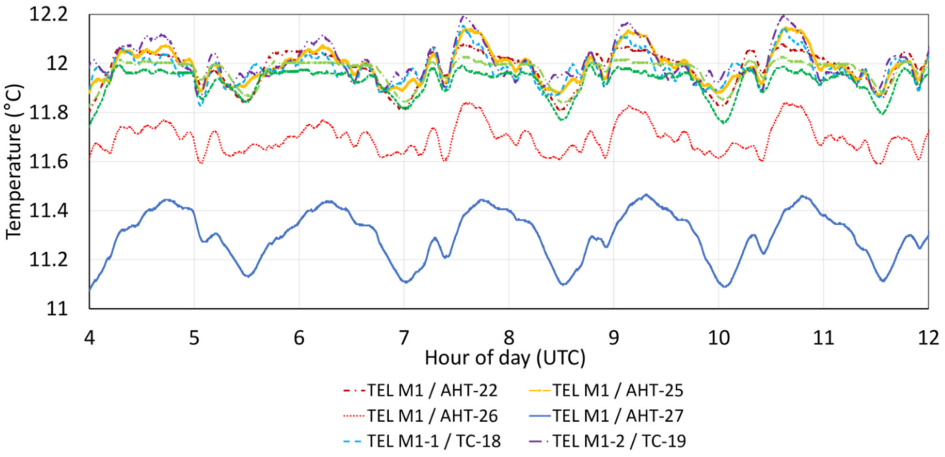

2.6 to 0.77 m·s^{-1} with the M1-temperature bias correction. For comparison a look-up table bias correction method (described at the end of this section using the previous week sample of $E(O-B)$, binned by argument of latitude and longitude is also shown in Figure 8. This method does reasonably well with a standard deviation of $E(O-B)$ of 1.05 m·s^{-1} (hence showing it was valid to apply in the early FM-B OSE, before the M1-temperature bias correction was available); however, the M1-temperature-dependent method is superior.

The likely explanation for the bias is that the temperature gradient variations (of only up to 0.3 K) cause small changes in the angle of incidence of the received atmospheric path laser light onto the spectrometers. The spectrometer response is sensitive to angular changes (particularly the Rayleigh spectrometer) which are misinterpreted as a Doppler frequency shift due to wind. Extensive evaluation confirmed that the vast majority of the Rayleigh-clear HLOS wind bias can be explained by the M1 temperature variations, rather than other sources of bias (given that the biases remaining after the correction are typically less than 1 m·s^{-1}). The Mie-cloudy winds also have an M1-temperature-dependent bias, but of the opposite sign to the Rayleigh and approximately a factor 10 less in magnitude. Despite the smaller effect it is however still beneficial to correct the Mie-cloudy winds.

Slowly varying thermal variations were already expected as a source of bias pre-launch along with for example, line-of-sight pointing knowledge errors, but it was assumed that the biases would be a perfectly harmonic function (to be corrected by a Harmonic Bias Estimator) with orbit phase angle (argument of latitude) and be

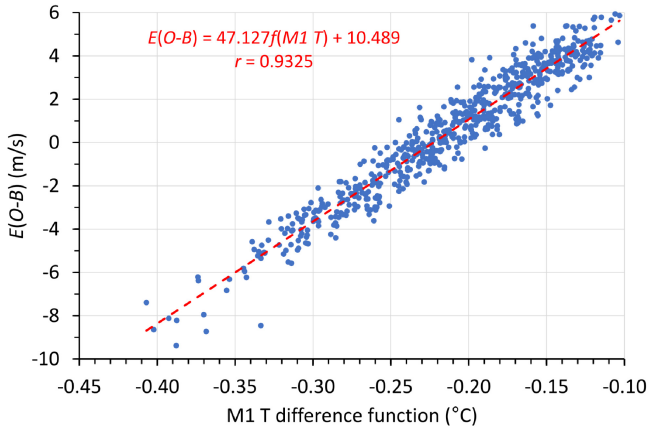

FIGURE 7 Aeolus L2B Rayleigh-clear HLOS wind bias $E(O-B)$ ($\mathrm{m\cdot s^{-1}}$) as a function of a M1 mirror temperature function (in this example the mean outer temperatures minus mean centre temperatures) using all the data available on 8 August 2019. Each data point is derived from a 2 min sample mean, over all altitudes. The dashed line is the linear fit and the coefficients (gradient and intercept) are written in the chart, as is the Pearson correlation coefficient r

of small magnitude. In practice the bias is not a simple harmonic function, instead it is strongly scene-dependent.

The robustness of the M1-temperature bias correction performance over long periods (e.g. months) was improved by allowing a flexible weighting (multiple linear regression) of all 15 thermistor readings, rather than the fixed (outer minus centre) gradient function. This was developed into operational software which will be described in a forthcoming in-depth article by the Aeolus DISC. The M1-temperature bias correction has been applied in operations since 20 April 2020; hence the step change improvement in global average bias shown in Figures 2 and 3. Twice-daily updates of the regression coefficients are performed to allow for the correction of a time-varying internal Rayleigh response dependent global offset bias.

It is quite common that NWP model information (from the past) is used to bias correct satellite data. Moreover, in this case, the physical explanation found through the M1-temperature-dependent bias makes it more acceptable. Note further that NWP fields can provide an HLOS wind for validation at all locations throughout an orbit, for which no alternative exists. Nevertheless, any localised ECMWF model wind bias, for example in the tropics, will act as a noise source in the global fit procedure. Any altitude-varying bias is not an issue, because all the O–B values throughout the profile are used; so effectively correcting to the altitude mean bias.

A typical example of the quality of L2B winds as a function of altitude with the M1-temperature bias correction applied for data measured on 2 August 2019 is shown in Figure 9. The figure shows error statistics as a function of altitude, in particular $E(O-B)$, estimated $\sigma(\epsilon_O)$, the mean of L2B processor estimated instrument noise $\sigma(\epsilon_{O,\mathrm{instr}})$ and the data count. Note that there are still residual biases with altitude, but they are generally small (within $\pm$ 1 $\mathrm{m\cdot s^{-1}}$).

The early FM-B period OSE (Section 2.3) did not use the M1-temperature bias correction method, because it was unavailable at the time. Instead bias correction was done via a look-up table of $E(O-B)$ binned by argument of latitude and longitude, as shown in Figure 4. For the Rayleigh-clear winds, 32 argument of latitude bins (11.25° each) and 10 longitude bins (36° each) were found to work well. For the Mie-cloudy winds we found that the longitude dimension to the look-up table was not required. The bias correction look-up tables were updated once per week, using the past week's O–B statistics. This was the method applied initially when Aeolus was operationally assimilated at ECMWF. The mid-2020 FM-B OSE period was determined by the availability of operational L2B data with the M1-temperature-dependent bias correction applied.

4 | NWP IMPACT ASSESSMENT

4.1 | OSE results

OSE results from two periods of the FM-B laser are shown, the first from the early FM-B period in August–December 2019 and the second from April to September 2020. A detailed description of the OSE design is provided in Section 2.3 and Table 1.

4.1.1 | How Aeolus changes the analysis

Figure 10 shows maps of the standard deviation of the analysis differences (experiment assimilating Aeolus Rayleigh-clear and Mie-cloudy minus the control) for zonal wind, for part of the mid-2020 FM-B period. The largest influence of Aeolus occurs in convectively active areas at 700, 250 and 150 hPa, and is most pronounced along the intertropical convergence zone (ITCZ), the South Pacific Convergence Zone (SPCZ), the Indian Ocean and to a lesser extent in the South Atlantic Convergence Zone (SACZ). This suggests that Aeolus is correcting the winds associated with convection that the background forecast does not represent well. Some areas of enhanced variance occur over the southeastern USA which is associated with the large background errors of mesoscale convective systems that typically occur in that time of the year shown (Rodwell *et al.*, 2013; Rennie, 2016). Similar geographical patterns exist for meridional wind and temperature, also for the early FM-B period (not

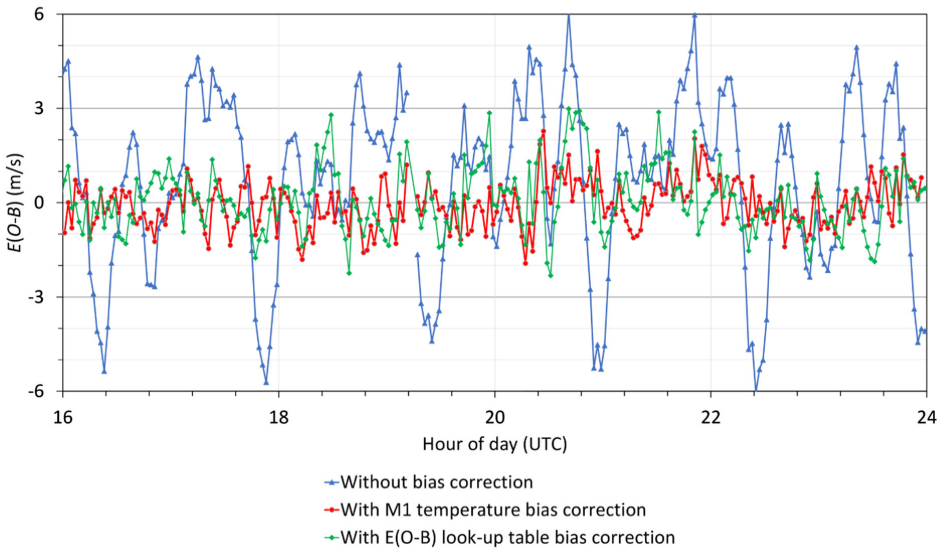

FIGURE 8 Time-series of Aeolus L2B Rayleigh-clear HLOS wind bias $E(O-B)$ (m·s^{-1}) every 2 min (using all vertical levels) between 1600 and 2400 UTC on 9 August 2019. The blue line with triangular markers shows the bias without any corrections, the red line with circular markers shows bias after the M1-temperature bias correction is applied and the green line with diamond markers shows bias after the previous week $E(O-B)$ look-up table bias correction method is applied. The M1-temperature bias correction linear regression was derived from the M1-temperature gradient function and O−B statistics of the previous day, that is, 8 August 2019, as shown in Figure 7

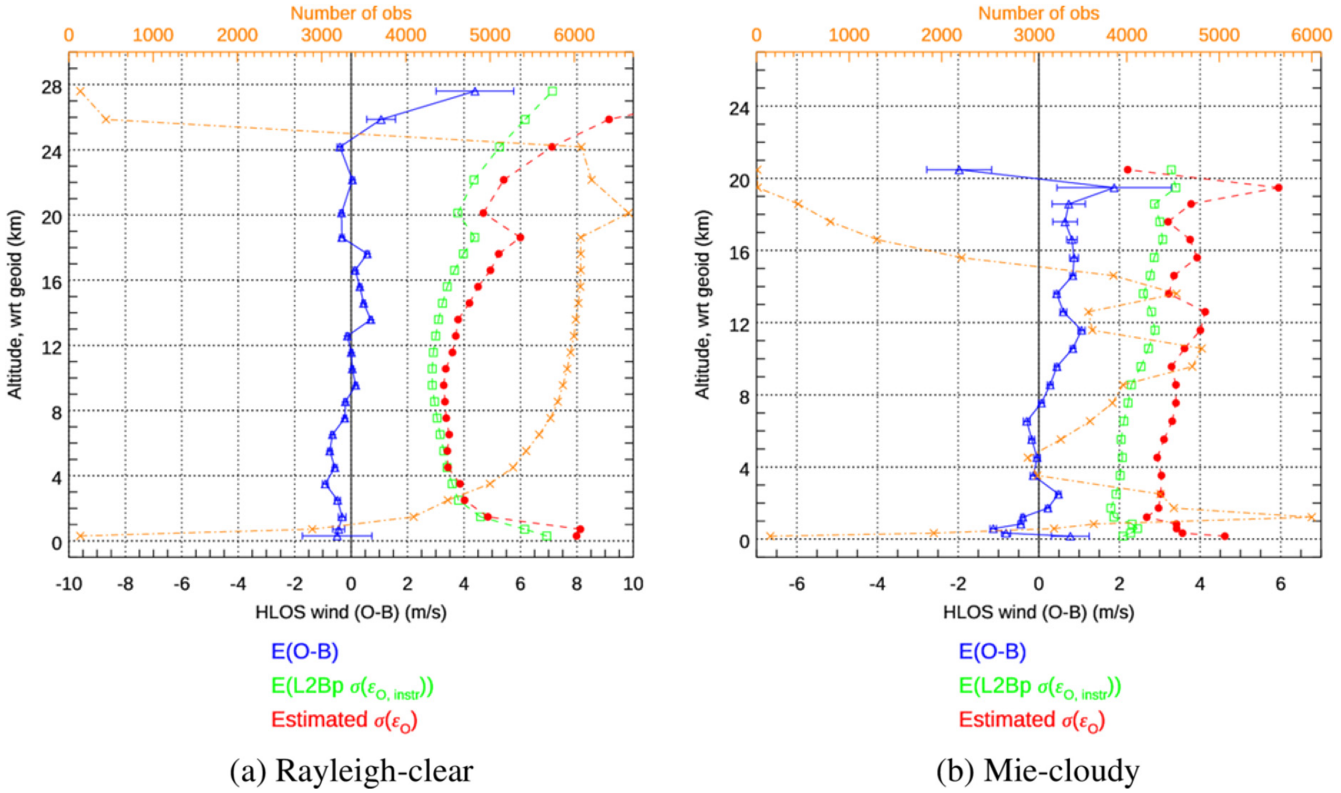

FIGURE 9 Error statistics of L2B HLOS winds with the M1-temperature bias correction applied for 14 orbits of data on 2 August 2019 as a function of altitude. (a) Rayleigh-clear and (b) Mie-cloudy HLOS winds. Blue triangles show $E(O-B)$, that is, bias; red circles show $\sigma(\epsilon_O)$, that is, estimated wind retrieval error; green squares show $E(\sigma(\epsilon_{O,\mathrm{instr}}))$, that is, the average L2B processor estimated instrument error, and orange crosses show the data count (associated with the top axis). QC of winds with L2B processor estimated error greater than 12 m·s^{-1} for the Rayleigh-clear and 5 m·s^{-1} for the Mie-cloudy was applied

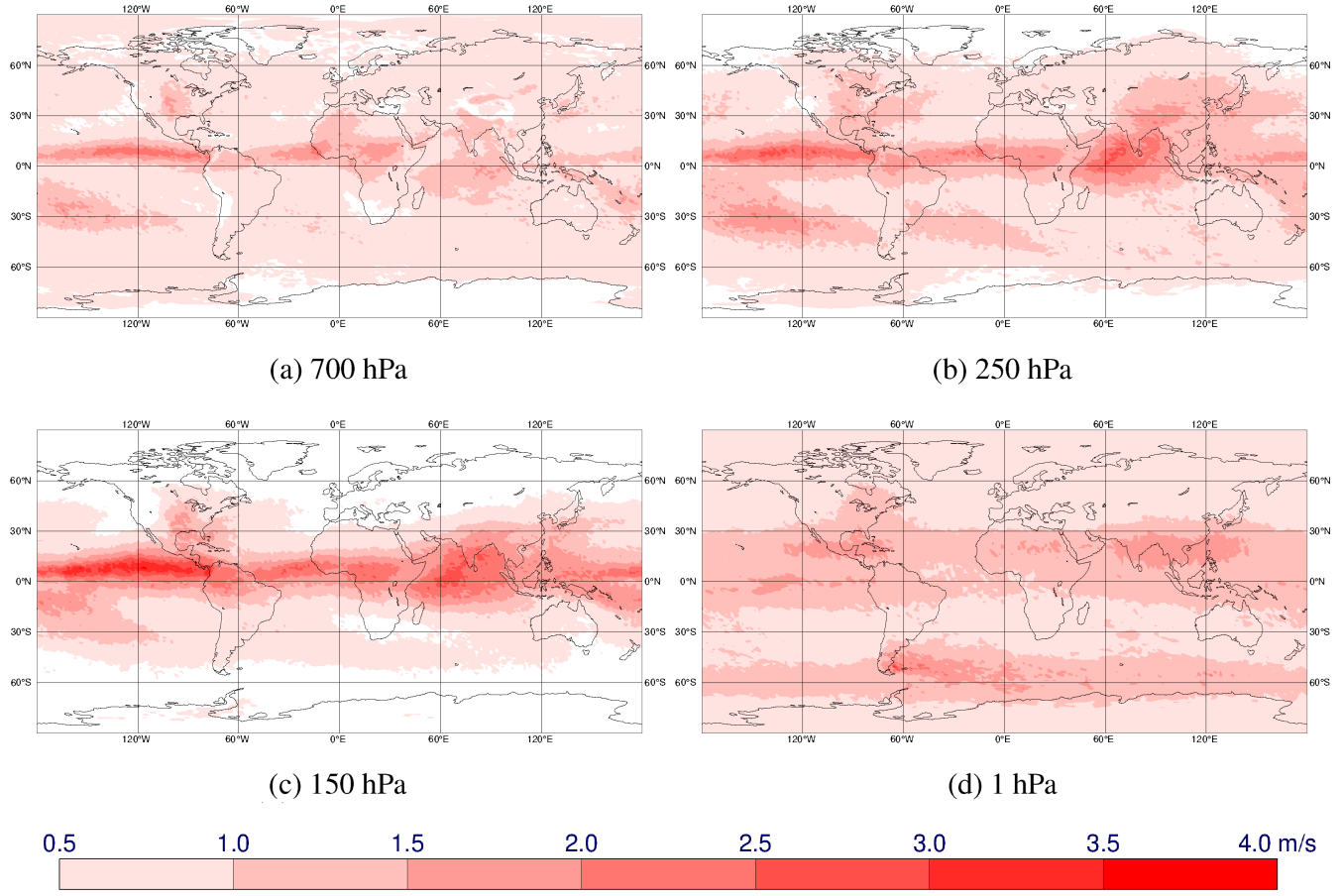

FIGURE 10 Maps of the standard deviation of the differences of zonal wind component ($m \cdot s^{-1}$) between the analysis using Aeolus HLOS winds (Rayleigh-clear and Mie-cloudy) and the control not using Aeolus for the period 4 April to 19 August 2020 (part of the mid-2020 FM-B period). For pressure levels: (a) 700 hPa, (b) 250 hPa, (c) 150 hPa and (d) 1 hPa

shown). The magnitude of the standard deviation is smaller in the extratropics for the mid-2020 period compared to early FM-B (not shown). This is likely due to the larger random errors for Aeolus Rayleigh-clear winds, as described in Section 3.1 and Table 3, and hence less influence on the analysis.

The largest magnitude changes to zonal wind occur at 150 hPa in the east Pacific ITCZ just north of the Equator, with standard deviation reaching 4 $m \cdot s^{-1}$. This is an area with large differences between wind analyses from various global NWP centres, for example: Baker *et al.*, 2014; Rennie, 2016. The standard deviation is also particularly large over the Indian subcontinent and surrounding ocean, which is likely associated with uncertainties during the Indian monsoon convection, which became active from around June 2020.

The wind field is also changed at very high altitudes (Figure 10d, 1 hPa, ~48 km), which is far above the direct measurements from Aeolus. This was also the case for the early FM-B period (not shown). The pattern which encircles the latitude band near 60°S suggests this relates to orographic gravity-wave activity downwind of Patagonia, similar to what was seen by Dahoui and McNally (2017). There are also more pronounced differences in the tropics which are likely to be associated with changes in the propagation of inertia–gravity waves. This suggests that lower-altitude Aeolus winds are affecting the propagation of gravity waves from the troposphere to the stratosphere by for example, changing the mean wind field.

Figure 11 shows examples of the mean change in the zonal wind analysis from assimilating Aeolus for the same period as used for Figure 10. Similar to Figure 10, the largest changes occur in the tropical troposphere, associated with the ITCZ with a pattern possibly suggesting a modification to the Walker Circulation. The tendency at 100 hPa is for Aeolus winds to make the zonal component larger at the Equator (i.e. more westerly) and more easterly at latitudes either side (near Africa and India), systematically adjusting the position and strength of the Tropical Easterly Jet associated with the Indian monsoon. Similar magnitude systematic changes occur as a result of Global Navigation Satellite System (GNSS) radio occultation and radiosonde assimilation. At higher altitudes

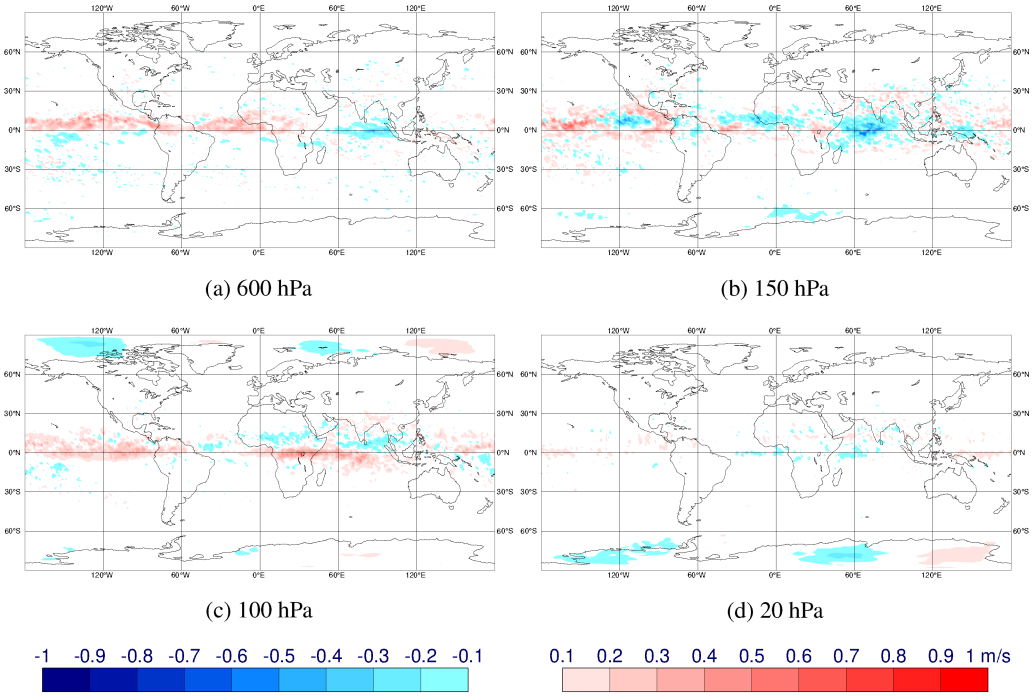

FIGURE 11 Mean of the differences of zonal component ($m \cdot s^{-1}$) at 100 hPa between the analysis using Aeolus HLOS winds (Rayleigh-clear and Mie-cloudy) and the control not using Aeolus for the period 4 April to 19 August 2020 (part of the mid-2020 FM-B period). For pressure levels: (a) 600 hPa, (b) 150 hPa, (c) 100 hPa and (d) 20 hPa

there are also systematic changes near the Poles – with an interesting pattern of alternating sign over Antarctica. The mean changes tend to persist throughout the forecast range (not shown). Similar magnitude changes also occurred in the early FM-B period.

4.1.2 | Short-range forecast fit to other observation types

The impact of Rayleigh-clear and Mie-cloudy winds on the short-range forecasts (up to 12 hr) as verified by the fit to a selection of observation types is shown in: Figure 12 for the early FM-B period (2 August to 31 December 2019) and in Figure 13 for the mid-2020 FM-B period (4 April to 20 September 2020). Figure 12 shows the impact from assimilating both Rayleigh-clear and Mie-cloudy (red lines) compared to only assimilating the Mie-cloudy winds (black lines). Figure 13 only shows the impact of assimilating both Rayleigh-clear and Mie-cloudy winds.

Aeolus improves the standard deviation of O–B departures (and hence short-range forecasts) to vector wind observations (radiosondes, aircraft and radar wind profilers) by typically less than 1%, with a reasonably consistent pattern for both periods. The positive impact is largest for winds in the tropics, peaking at 150 hPa (around 1.3% for mid-2020 FM-B period) but improvement exists throughout the troposphere and lower stratosphere. The Southern Hemisphere extratropics (SH) positive impact is present in the troposphere and lower stratosphere, peaking at 250 hPa in the mid-2020 FM-B period. The SH impact is stronger in the mid-2020 period (1% rather than 0.5% for vector wind); perhaps because it covers the more dynamic SH winter period. The Northern Hemisphere extratropics (NH) impact is more neutral, but there is 0.2% positive impact for global radiosonde temperature (which is dominated by NH radiosondes).

Figures 12 and 13 shows that Aeolus improves the fit to many other satellite observations as well, such as a consistent improvement relative to Advanced Technology Microwave Sounder (ATMS) global microwave temperature sounding channels (6–15) and humidity-sensitive channels (18–22). In both periods there is a slight degradation in fit to AMSU-A channel 13 (peaking at ~35 km altitude) in the NH (not shown). The fit to the high vertical resolution (mostly temperature) information of GNSS radio occultation is improved by 0.6–0.8% in the upper troposphere and lower stratosphere (~14–15 km) in the global average and 1–2% in the tropics (not shown), and positive impact is seen throughout much of the troposphere and lower stratosphere (similar to the improvements with respect to radiosondes). The tropical GNSS radio occultation impact was stronger in the early FM-B period. The change relative to Atmospheric Motion Vectors (AMVs) is positive, but only a small improvement. The

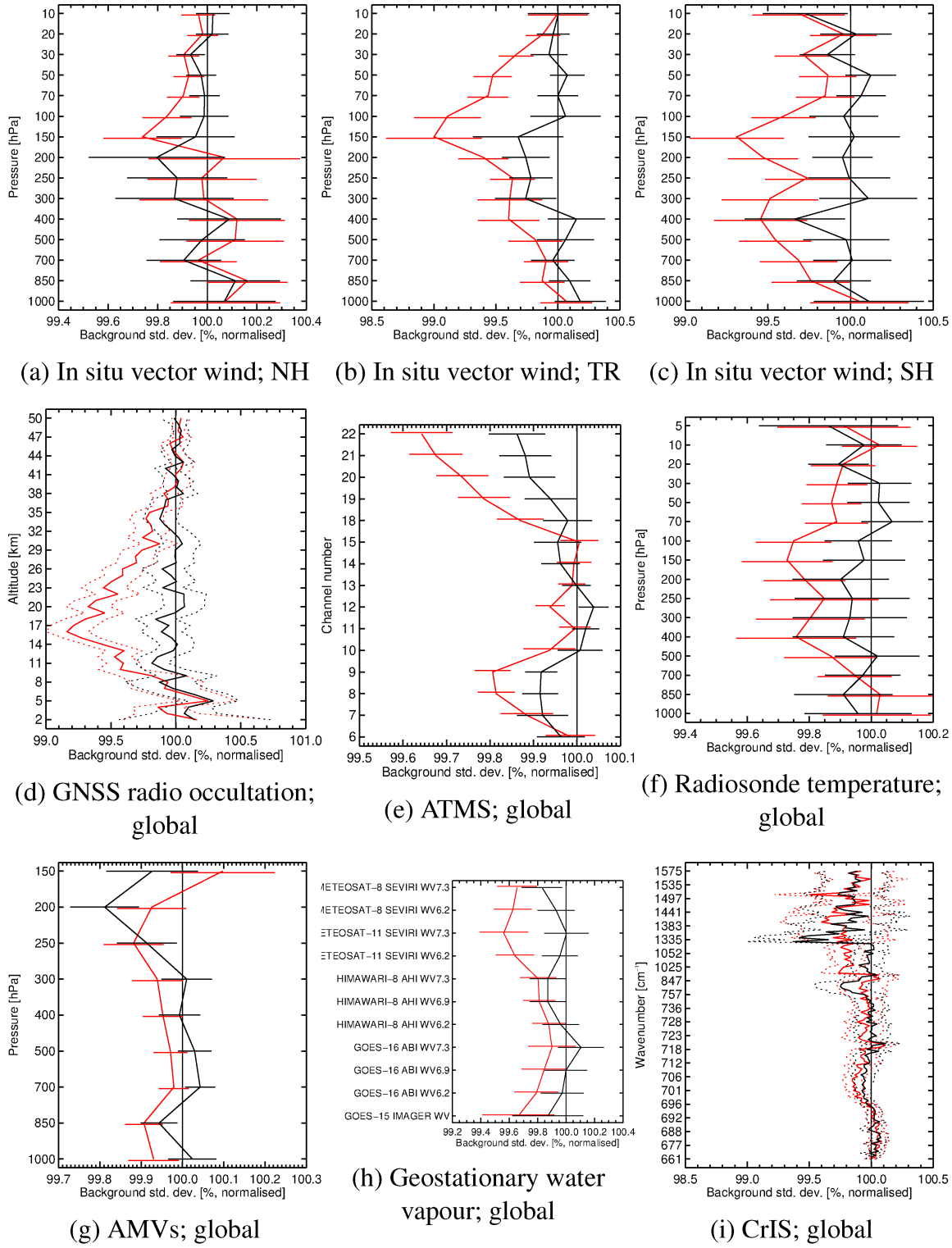

FIGURE 12 Change in O−B departure standard deviation resulting from assimilating Aeolus HLOS winds for the early FM-B period (2 August to 31 December 2019). The red lines show impact from assimilating both Rayleigh-clear and Mie-cloudy winds, and the black lines are from assimilating Mie-cloudy only. The results are normalised so that the control is 100%; values below 100% show an improved fit from assimilating Aeolus and above 100% show a degraded fit. The observation types are (a) *in situ* vector winds in the NH (Northern Hemisphere extratropics), (b) *in situ* vector winds in the TR (tropics), (c) *in situ* vector winds in the SH (Southern Hemisphere extratropics), (d) global GNSS radio occultation data, (e) global ATMS data, (f) global radiosonde temperature, (g) global AMVs, (h) geostationary water vapour channels and (i) global CrIS data. Horizontal bars (and dashed lines in (d) and (i)) show the 95% confidence range (Student's *t*-test)

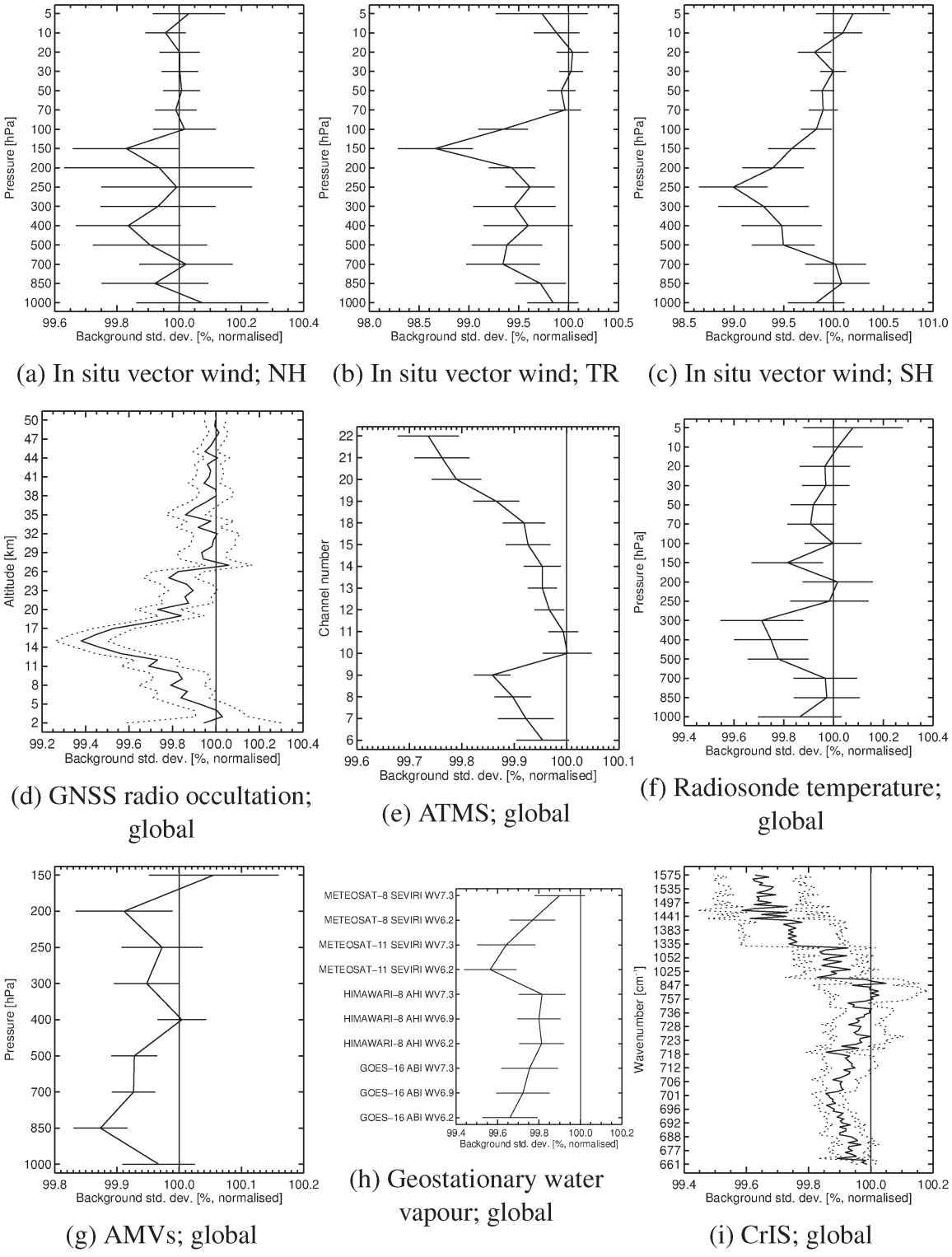

FIGURE 13 Similar to Figure 12, showing the impact of assimilating Aeolus HLOS both Rayleigh-clear and Mie-cloudy winds for the mid-2020 FM-B period (4 April to 20 September 2020)

fit to geostationary water vapour imagery is consistently improved, as is the fit to various microwave humidity sounders (not shown). There is a slight degradation in both periods with respect to NH aircraft humidity near the surface; but not seen against radiosonde humidity. Relative to the infrared hyperspectral sounding instrument, CrIS (Cross-track infrared sounder), Aeolus improves the fit to temperature sensitive channels in the upper troposphere and lower stratosphere and in channels sensitive to the surface temperature and humidity. There are also

mprovements relative to scatterometer winds and wave height altimeter data (not shown).

Based on the early FM-B period (Figure 12) by comparing the impact from assimilating both Rayleigh-clear and Mie-cloudy with only assimilating Mie-cloudy, it is evident that the Rayleigh-clear winds are providing the bulk of the short-range positive impact, particularly in the tropics and SH.

In general, assimilating Aeolus provides valuable improvements in the short-range forecast of wind, temperature and humidity. Overall, the impact was larger for the early FM-B period. The magnitude of the short-range impact is consistently of a good magnitude for one satellite instrument, when compared to other satellite data shown from ECMWF OSEs in the past few years, for example, compared to the results in Bormann *et al.* (2019).

Aeolus assimilation leads to small (slightly positive) changes in the mean O–B departures relative to tropical *in situ* wind data (not shown). This indicates that the mean analysis changes are on average improvements. This is reassuring given that the bias correction of Aeolus relies on the potentially biased ECMWF background winds (but we know they are small for long time-scale or global averages).

4.1.3 | Medium-range forecast impact

Figure 14 shows the normalised change in vector wind root-mean-square (RMS) error when assimilating Aeolus (both Rayleigh-clear and Mie-cloudy) for the early FM-B period, for forecast range of 2 to 5 days. Negative values (cyan/blue colours) indicate a reduction in error due to Aeolus, whereas positive values (yellow/red colours) indicate an increase in errors. The verifying analysis is the ECMWF operational analysis. The impact on 2- to 5-day forecasts is predominantly positive with statistical significance (cross-hatching) in the tropical troposphere and polar regions; the percentage improvements are on the order of 1–2%. The extratropical impact by day 5 is more neutral (apart from South Pole stratosphere region) but remains positive in the tropical troposphere and lower stratosphere. Similar patterns and magnitude of impact is seen for the temperature and relative humidity fields (not shown).

Figure 15 shows the impact of Mie-cloudy winds only, using vector wind verification. When comparing with Figure 14 it is evident that it is very beneficial to assimilate both Rayleigh-clear and Mie-cloudy winds. It is seen that the strong impact in the tropics is primarily due to the Rayleigh-clear winds rather than the Mie-cloudy winds; however, the Mie-cloudy winds provide strong impact in polar regions.

Figure 16 shows the same verification metric but for the mid-2020 FM-B period (4 April to 20 September 2020). This OSE used M1-temperature bias corrected L2B data (see Section 3.4). It was demonstrated in a 16-day OSE that the M1-temperature bias correction method provided greater positive impact than the look-up table method, which corroborates the better performance of the M1-temperature bias correction compared to the look-up

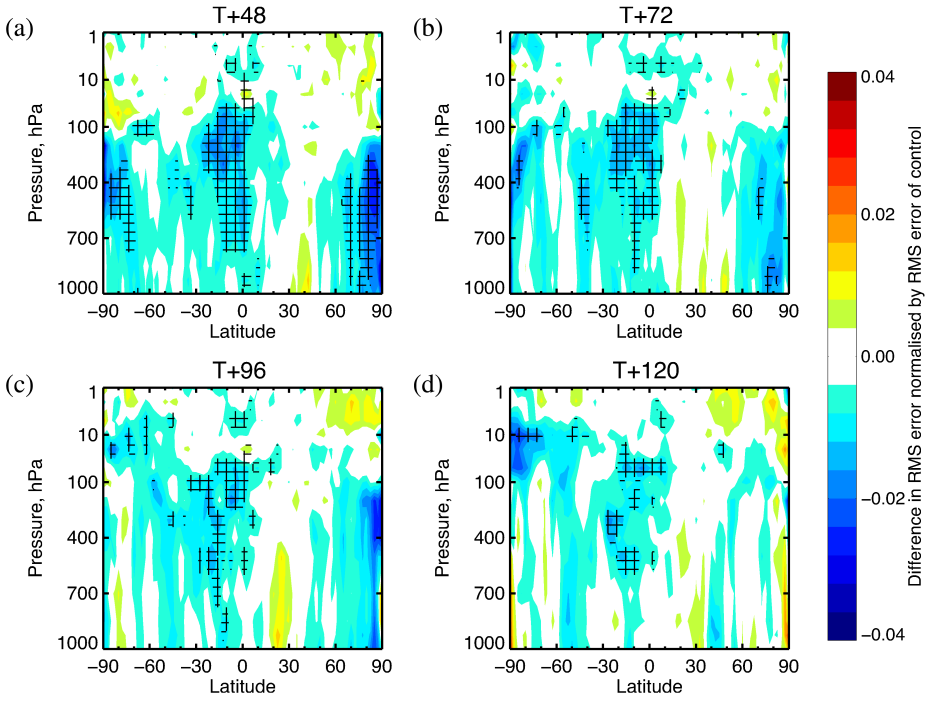

FIGURE 14 Zonal average normalised change in vector wind RMS error for forecast range of (a) 48, (b) 72, (c) 96, and (d) 120 hr for the early FM-B period, 2 August to 31 December 2019. Coming from the addition of Aeolus (Rayleigh-clear and Mie-cloudy) in an ECMWF IFS system representative of the operational configuration used in December 2020 (between 284 and 303 samples). Cross-hatching indicates the 95% confidence level. Verification against operational analyses. Negative values indicate Aeolus wind data is improving the forecasts

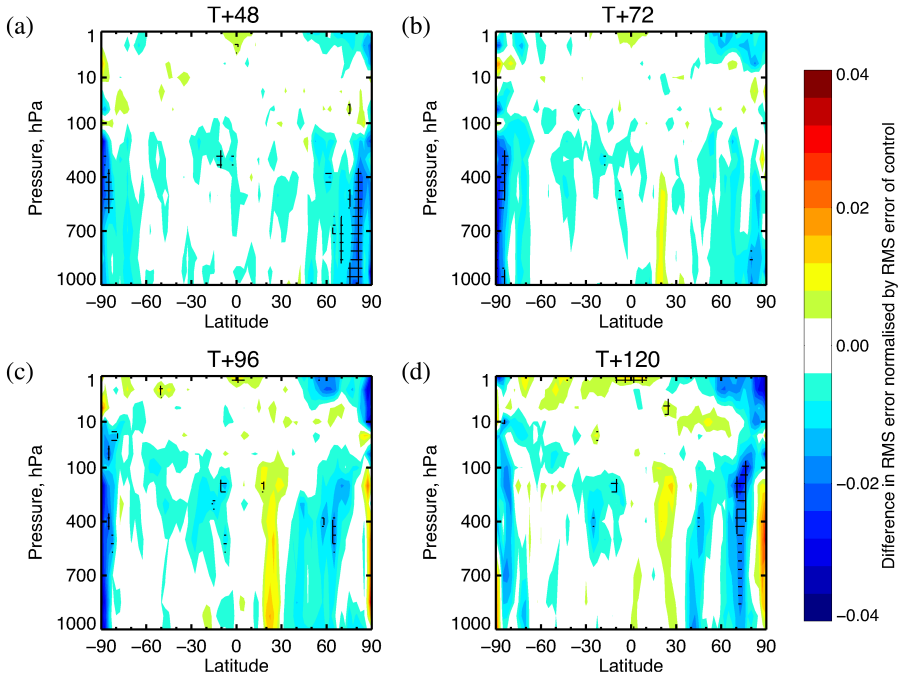

FIGURE 15 As in Figure 14, but from the addition of Mie-cloudy only

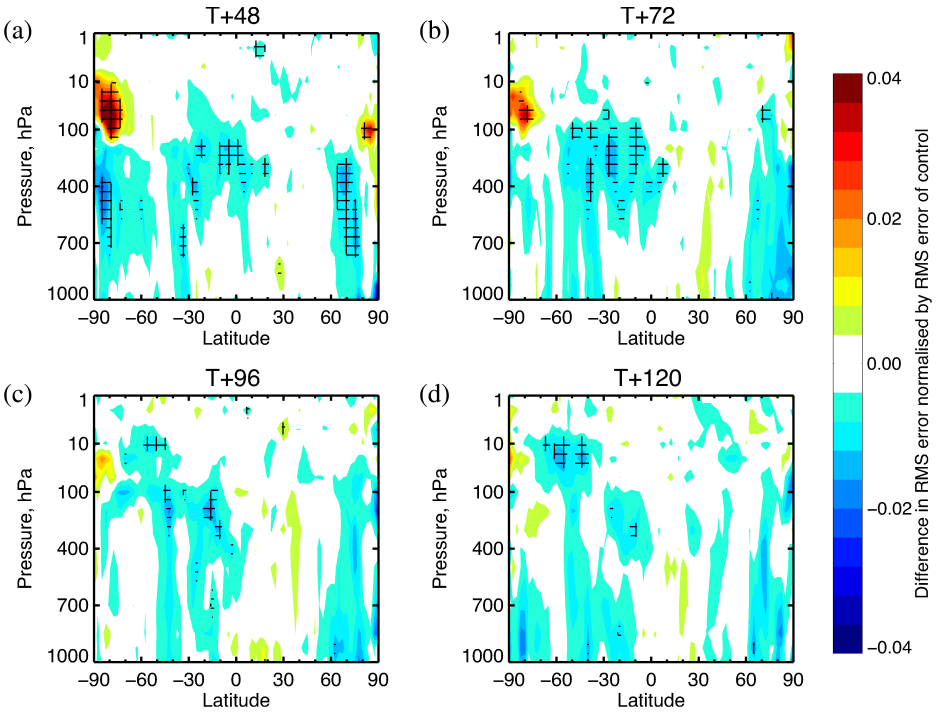

FIGURE 16 Zonal average normalised change in vector wind RMS error for forecast range of (a) 48, (b) 72, (c) 96 and (d) 120 hr for the mid-2020 FM-B period. Coming from the addition of Aeolus (Rayleigh-clear and Mie-cloudy) in an ECMWF system representative of the operational configuration in June 2020 (between 320 and 339 samples). Cross-hatching indicates the 95% confidence level. Verification against own-analyses. Negative values indicate Aeolus is improving the forecasts

table method shown in Figure 8. The verification reference in Figure 16 is chosen to be own analyses, due to Aeolus being operationally assimilated during this period. The impact on 2- to 5-day forecasts is mostly positive with statistical significance in the tropical troposphere and polar areas. The percentage improvements are on the order of 1% in the tropics and poles which is smaller than the early FM-B period. Since the Rayleigh-clear winds gave the bulk of the tropical impact in the early FM-B OSE, the increased Rayleigh-clear wind noise in mid-2020 probably accounts for the smaller tropical impact. The positive impact has similar geographical patterns to that shown for early FM-B.

Figure 16 shows some apparent negative impact at 2–3 days in the polar lower stratosphere, but this is not evident in verification against ECMWF operational analysis, Figure 17, which combined with the positive impact seen in short-range forecast fit to observations (Figure 13) suggests it is a well-known artefact of verification against own analyses when Aeolus is making large changes to the

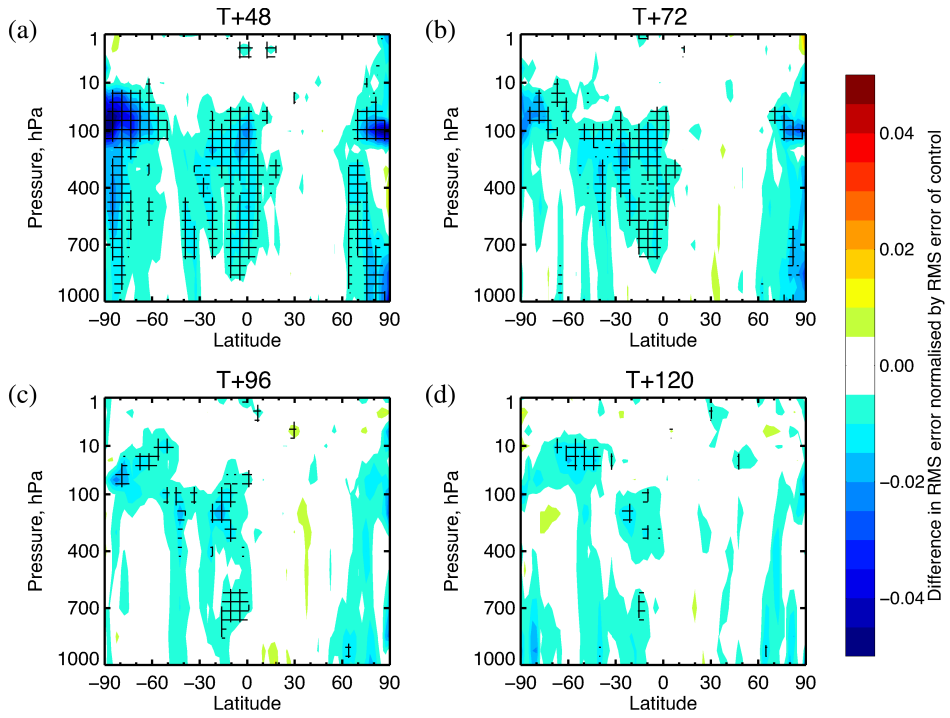

FIGURE 17 As in Figure 16 but verified against operational analyses

analysis. It is interesting that Figure 11d shows notable systematic increments made by Aeolus over Antarctica at 20 hPa, which matches where the apparent negative impact occurs. The positive impact with respect to the operational analysis in Figure 17 looks a lot stronger than with respect to own analyses, shown in Figure 16, for days 2 to 4, but by day 5 they look similar.

Positive impact is also evident in the mass fields (temperature and humidity). Figure 18 shows the 500 hPa geopotential height for (a) the early FM-B and (b) the mid-2020 FM-B periods. The positive impact is typically less than 1% for the first few days, but then statistical significance is lost. The impact of Aeolus on tropical temperature is strong, as shown in Figure 19. At 200 hPa statistical significance up to day 4–5 for both periods is shown. The tropical upper troposphere and lower stratosphere impact from Aeolus was particularly strong for the early FM-B period, as shown by temperature verification at 50 and 100 hPa in Figure 19; there is statistical significance out to day 9 at 50 hPa (~20 km). The artefacts, discussed above, when verifying Aeolus experiments against operational analyses without Aeolus data assimilated are evident at 12 and 24 hr forecast ranges.

By day 5 there is positive impact in the SH stratosphere at 10–100 hPa (16–30 km) in both OSE periods, as shown in Figures 14 and 16. The mechanism for this impact at higher altitudes than Aeolus observes could be via lower-altitude improvements to the mean wind field leading to improved propagation of gravity waves from the troposphere to stratosphere (Section 4.1.1).

In general, Aeolus shows useful improvements in the medium-range forecasts of wind and temperature that are consistent with the short-range forecast impact relative to observations. So also, in the medium range, the magnitude of the impact is good for one satellite instrument, as compared to other satellite data shown from ECMWF OSEs in the past few years, for example, Bormann *et al.* (2019).

4.2 | FSOI results

Figure 20 is a time-series of the Aeolus FSOI results from the ECMWF operational data assimilation for the period 9 January to 20 September 2020. It shows global daily FSOI absolute values summed over all assimilated Aeolus winds, with an 8-day rolling average applied to reduce noise. The negative of FSOI is plotted, so positive values are positive impact and impact is split into Mie-cloudy, Rayleigh-clear only and the summation of both. There are approximately 130,000 Rayleigh-clear and 50,000 Mie-cloudy winds assimilated per day.

Note there are periods of reduced impact due to Aeolus not being assimilated during instrument tests by ESA (mid-April, late May, early July and late September). The Rayleigh-clear impact has reduced with time, which is probably due to increasing noise (~0.5 $m \cdot s^{-1}$ noisier in September compared to January 2020; see Figure 2). The Mie-cloudy impact increased in April 2020, which is due to the introduction of new processing software, providing ~5,000 more L2B Mie-cloudy winds per day.

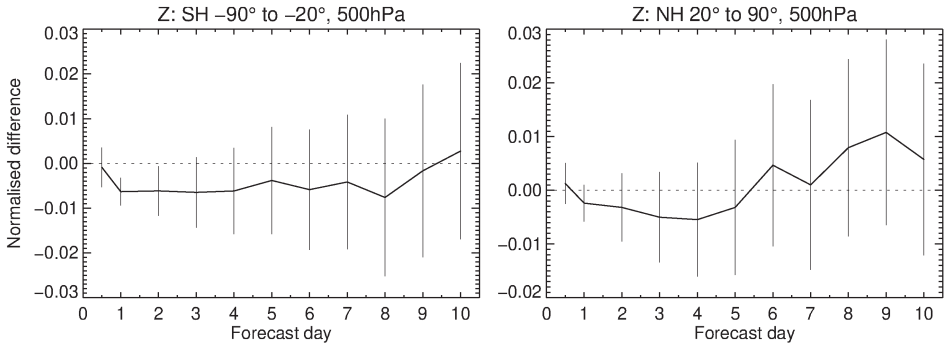

FIGURE 18 Normalised change in RMS error in 500 hPa geopotential for (a) the early FM-B period and (b) the mid-2020 FM-B period from the addition of Aeolus (Rayleigh-clear and Mie-cloudy). SH is shown on the left and NH on the right. Negative values indicate Aeolus is improving the forecasts. Verification against operational analyses for (a) and against own-analyses for (b). Confidence range 95% indicated by vertical bars

Note however that both Rayleigh and Mie FSOI trends may have been influenced by significant changes in the rest of the operationally assimilated observing system if those observations affect the analysis in similar ways to Aeolus. Such influences are likely to come from additional GNSS radio occultation data from COSMIC-2 on 25 March 2020 which also has a strong impact on tropical winds (Ruston and Healy, 2020). Also, the significant reductions in aircraft observation numbers due to Covid-19 from late March 2020 has increased the Aeolus impact in the areas where they are missing. The Aeolus observation numbers increased by 12% from early March to early April 2020, with an average impact increase per Aeolus observation of 28%. In terms of global FSOI the combined Rayleigh-clear and Mie-cloudy impact are similar in magnitude since April 2020.

Figure 21 maps the vertical profile average FSOI per observation for Rayleigh-clear and Mie-cloudy winds, partitioned by orbit phase. A standout feature for both the Rayleigh-clear and Mie-cloudy is the reduced impact in certain longitude bands centred over Asia and the Americas. This was confirmed to be associated with the UTC validity time of the Aeolus winds in those longitude bands lying close to the start of the ECMWF 12 hr data assimilation window. Observations that occur near the end of the data assimilation window have much larger positive impact than those at the start, as demonstrated in the OSE context by McNally (2019).

Outside the longitude bands of reduced impact, for Rayleigh-clear winds the largest impact per observation is in the tropics; and to a lesser extent over extratropical oceans. The Mie-cloudy impact per observation is large both in the tropics and extratropical oceans, such as the South Atlantic Convergence Zone.

The FSOI impact per observation of the Mie-cloudy is roughly twice that of Rayleigh-clear. This is probably due to: the smaller Mie-cloudy assigned random error (~28% smaller); the larger average background error (via EDA spread) at Mie-cloudy geolocations (~20% bigger); and the higher density of Mie-cloudy observations within a certain area due to higher resolution.

Figure 22 shows zonal average plots of mean FSOI per observation for Rayleigh-clear and Mie-cloudy HLOS winds (only for descending orbits, due to ascending being similar); for the period 9 January 2020 to 1 September 2020. The Rayleigh-clear winds have the largest impact in the tropics, peaking at ~250–110 hPa (~10–15 km); agreeing with the short-range forecast improvements relative to radiosonde winds and GNSS radio occultation shown in Section 4.1.2. There is also Rayleigh impact in the SH polar troposphere. The Mie-cloudy impact appears larger in SH and tropics.

The relative FSOI per observation instrument type (summed FSOI by instrument divided by the summed FSOI from all observations) was assessed. Aeolus L2B winds score highly, coming seventh out of around 80

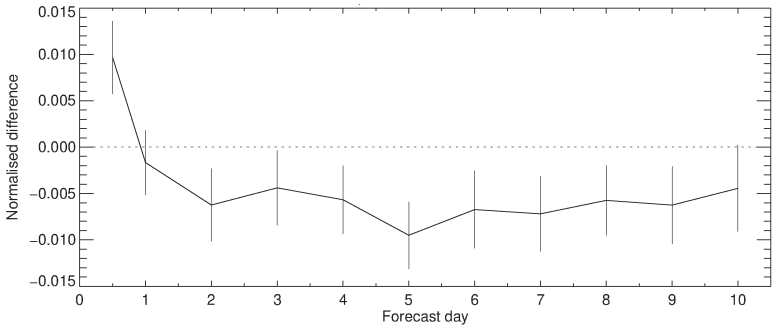

(a) Early FM-B; temperature at 50 hPa

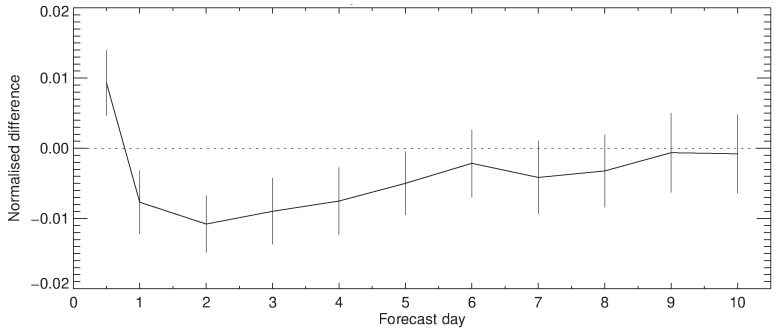

(b) Early FM-B; temperature at 100 hPa

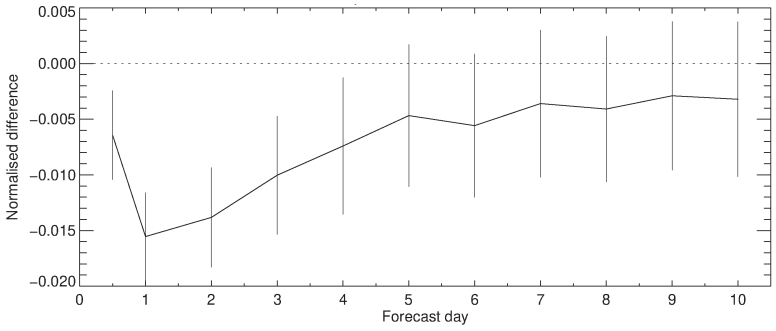

(c) Early FM-B; temperature at 200 hPa

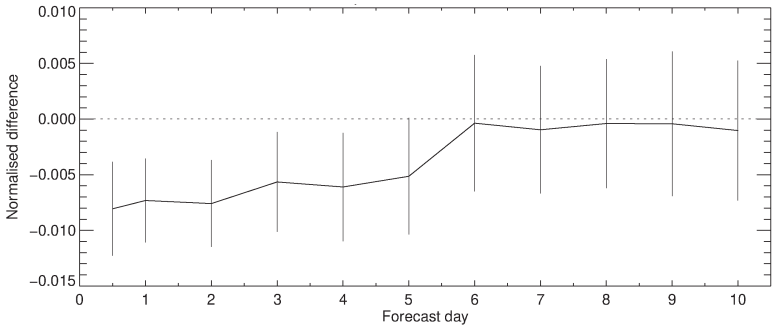

(d) Mid-2020 FM-B; temperature at 200 hPa

FIGURE 19 Normalised change in temperature RMS error for the tropics (within ±20° latitude) for (a) the early FM-B period at 50 hPa, (b) early FM-B period at 100 hPa, (c) early FM-B period at 200 hPa and (d) mid-2020 FM-B period at 200 hPa. All from the addition of Aeolus (Rayleigh-clear and Mie-cloudy). Verification against operational analysis, apart from (d) which is verification against own-analysis. Confidence range 95% indicated by vertical bars

instruments, providing about 3.2% of the total FSOI, for the period 9 January to 29 June 2019, during which ECMWF cycle CY46R1 was operational. Larger relative FSOI was provided by the following space-based instruments: IASI (Infrared Atmospheric Sounding Interferometer) radiances flying on the three MetOp satellites, AIRS (Atmospheric Infrared Sounder) radiances on the Aqua satellite and the NPP (National Polar-orbiting Partnership)

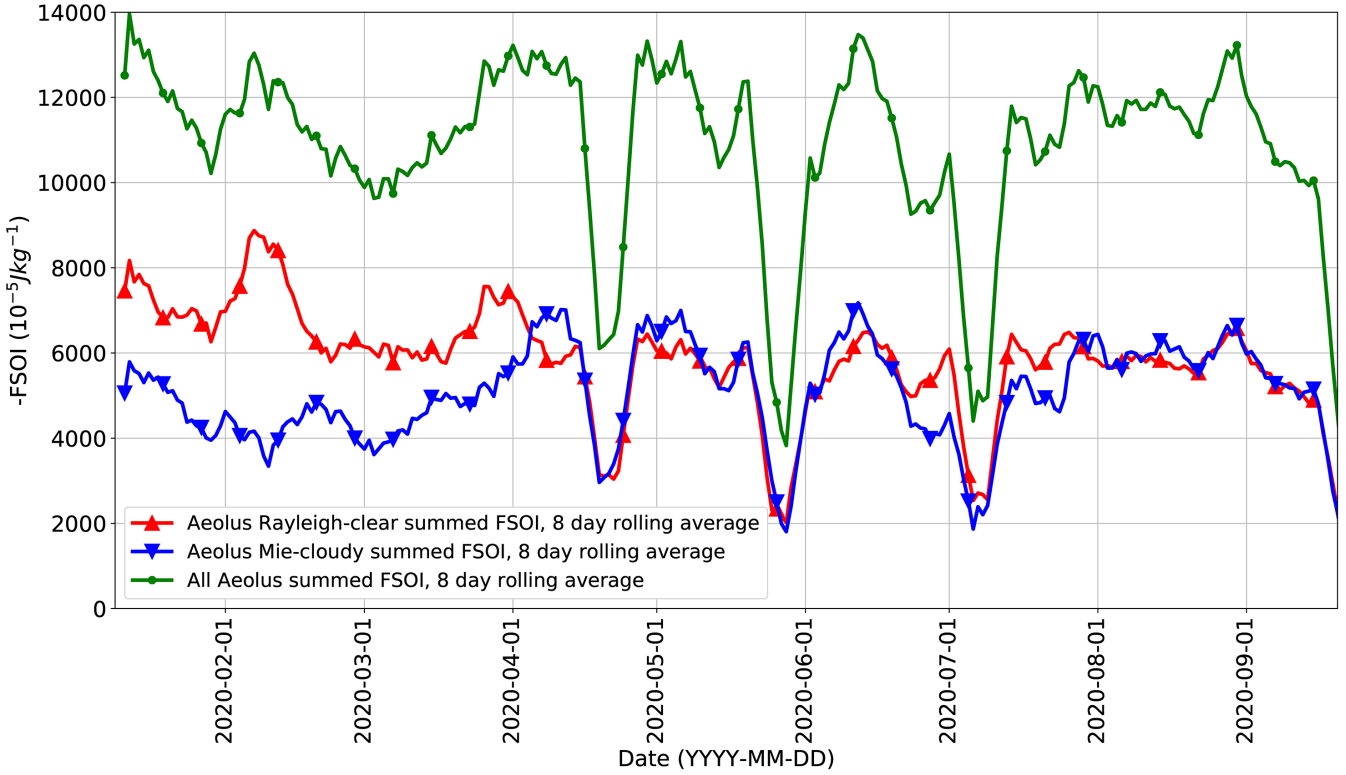

FIGURE 20 Time-series of global, daily summed FSOI for Aeolus L2B HLOS winds, for the period 9 January to 20 September 2020. Eight-day rolling average applied to reduce noise. The *y*-axis is the negative of the FSOI and therefore positive values represent positive impact

ATMS (Advanced Technology Microwave Sounder) radiances. Aeolus' FSOI impact is however rather similar in magnitude to a hyperspectral infrared sounder. The largest impact overall came from WIGOS (WMO Integrated Global Observing System) AMDAR (Aircraft Meteorological DAta Relay), which are *in situ* commercial aircraft observations of wind, temperature and humidity.

With Aeolus' high absolute FSOI impact, the FSOI per observation ranks highly compared to other satellite data given it accounts for less than 1% of observations assimilated (~86,000 per 12 hr assimilation window). The FSOI per observation is second only to scatterometer ocean surface wind data for this period.

5 | DISCUSSION

ESA's mission requirements document for Aeolus (ESA, 2016) states a required standard deviation of error (random error) of 2.5 m·s^{-1} in the free troposphere and bias less than 0.7 m·s^{-1}. Aeolus' HLOS wind precision (1-σ) is found to be typically 4.0–5.5 and 3.0 m·s^{-1} for the Rayleigh-clear and Mie-cloudy HLOS winds respectively in the free troposphere (see Table 3), which is significantly larger than the ESA mission requirements. Compared to the WMO's OSCAR (Observing Systems Capability Analysis and Review Tool) criteria for horizontal winds in global NWP (WMO, 2018), the Rayleigh-clear winds are better than the free troposphere "threshold" value (5.7 m·s^{-1} when accounting for the conversion from vector wind to HLOS wind error), but not reaching the "breakthrough" (2.1 m·s^{-1}). The Rayleigh-clear winds are worse than even the "threshold" of 3.5 m·s^{-1} in the UTLS (upper-troposphere, lower stratosphere) and PBL (planetary boundary layer); however, the Mie-cloudy winds meet the "threshold".

The main reason for not (yet) achieving the mission requirements on precision is the lower than expected atmospheric path signal levels (by a factor ~2–3 in the early mission phase), due to issues with radiometric performance, as confirmed by Aeolus DISC investigations (Reitebuch *et al.*, 2020a; 2020b). Also, with lower useful signal, the solar background noise becomes a more dominant error source for the Rayleigh-clear winds. The cause of the lower than expected signal levels and ways to mitigate it are still under investigation by ESA, the space industry and the Aeolus DISC.

With typical Aeolus useful atmospheric signal levels (S), the Rayleigh-clear σ_O is significantly larger than σ_B (by factor ~ 2.0–2.8). From simple scalar data assimilation theory, the analysis standard error (σ_A) as a function of the

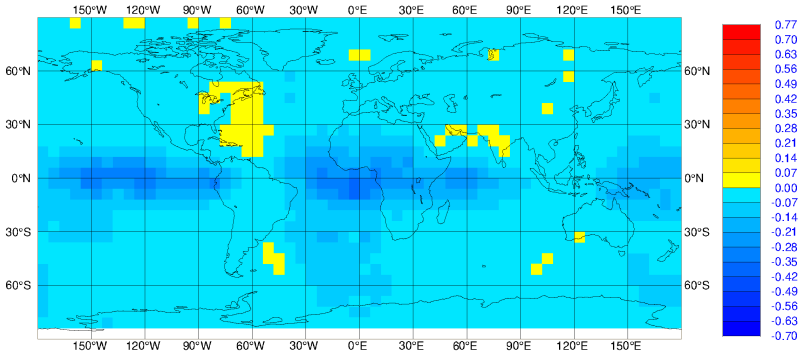

(a) Rayleigh-clear, ascending

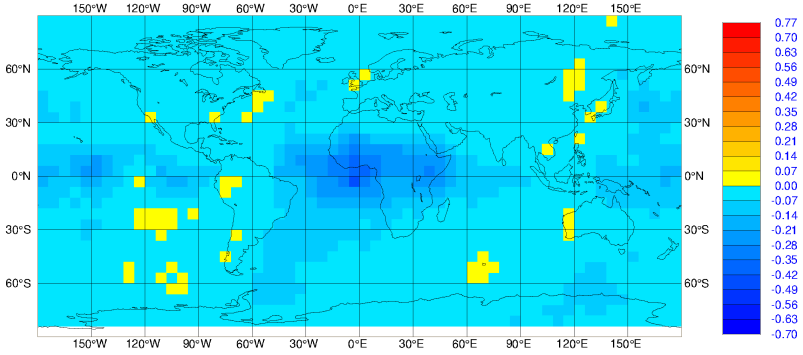

(b) Rayleigh-clear, descending

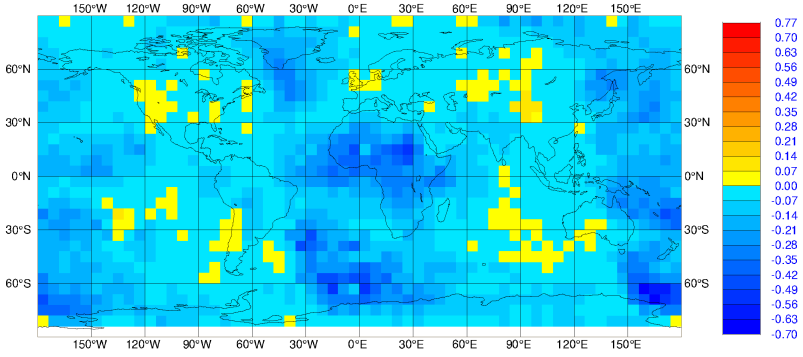

(c) Mie-cloudy, ascending

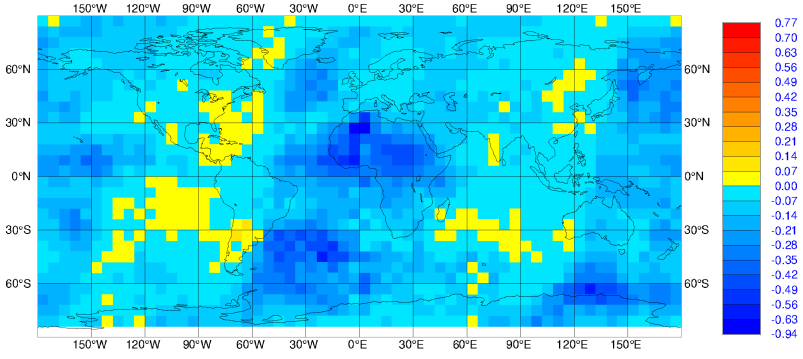

(d) Mie-cloudy, descending

FIGURE 21 Maps of profile average, mean FSOI per observation (10^{-5} J·kg^{-1}) for the period 9 January to 1 September 2020 for (a) Rayleigh-clear in ascending orbit phase, (b) Rayleigh-clear in descending orbit phase, (c) Mie-cloudy in ascending orbit phase and (d) Mie-cloudy in descending orbit phase. Negative values (blue) are positive impact

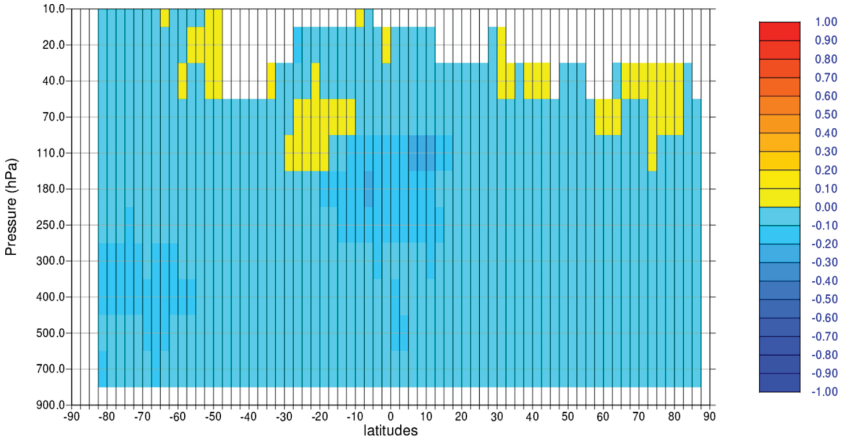

(a) Rayleigh-clear, descending

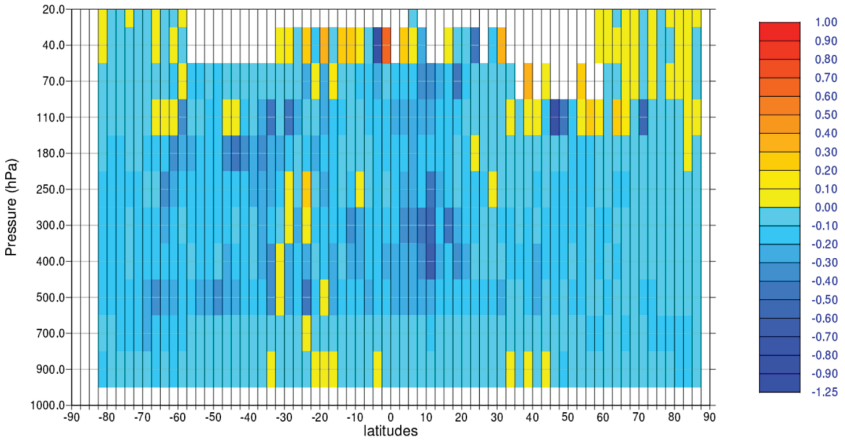

(b) Mie-cloudy, descending

FIGURE 22 Zonal average mean FSOI per observation (10^{-5} J·kg^{-1}) for the period 9 January to 1 September 2020 for (a) Rayleigh-clear in descending orbit phase and (b) Mie-cloudy in descending orbit phase. Negative values (blue) are positive impact

background (σ_B) and observation (σ_O) standard error is:

$$\sigma_A = \sqrt{\frac{\sigma_O^2 \sigma_B^2}{\sigma_O^2 + \sigma_B^2}}.$$

A measure of the relative NWP impact of a Rayleigh-clear wind on the analysis error $(1 - \frac{\sigma_A}{\sigma_B})$ can be approximated using a Taylor expansion for small $\left(\frac{\sigma_B}{\sigma_O}\right)^2$, using $\sigma_O \propto \frac{1}{\sqrt{S}}$ to give:

$$1 - \frac{\sigma_A}{\sigma_B} = 1 - \frac{1}{\sqrt{1 + \left(\frac{\sigma_B}{\sigma_O}\right)^2}} \approx \frac{1}{2}\left(\frac{\sigma_B}{\sigma_O}\right)^2 \propto S.$$

Therefore, the Rayleigh-clear wind analysis impact is predicted to be approximately linearly proportional to the useful atmospheric signal. Therefore, if Aeolus had achieved a factor 2–3 more useful signal (to bring it in line with mission requirement random errors), then this simplified univariate formulation predicts that the analysis impact from the Rayleigh-clear winds would be ~2–3 times larger. However, in the complex IFS 4D-Var data assimilation with many observation types used and the subsequent forecast, it is too simplistic to conclude such an impact would apply. It should be noted that the Rayleigh-clear impact was shown to be smaller in the noisier mid-2020 period compared to early FM-B period, agreeing with the assertion that we are in the regime where the impact depends on signal levels. A follow-on investigation into how the forecast impact (e.g. FSOI or another OSE forecast impact metric) varies with Rayleigh useful signal could be performed to determine if a linear relationship applies in practice; using reprocessed data with a large range of signal levels, for example, the FM-B laser period. However, some extrapolation would still be required to predict the forecast impact for the yet unattained signal levels required to achieve the mission requirement random errors.

Despite the larger than expected Rayleigh-clear random errors, it was demonstrated that Aeolus still gives a very useful positive impact in ECMWF's global NWP system. The positive impact is thought to be aided by the fact that the global observing system is still significantly lacking in other sources of global wind profile data.

The Mie-cloudy wind random error does not have such a simple relationship on signal levels. Its random error estimates are closer to the mission requirements in the free troposphere due to the strong backscatter from ice and water clouds, meaning the random errors are more sensitive to other effects, such as representativeness errors due to the scattering from small-scale cloud features.

It was demonstrated with the ECMWF data assimilation system by Horányi *et al.* (2015b) that using HLOS winds (calculated from *in situ* wind observations) with artificial biases that are a large fraction of the standard deviation of observation error causes a considerable reduction in positive impact, and with sufficiently large bias an overall negative impact can result. It is therefore very important to deal with biases in the data assimilation of Aeolus, if not already corrected in the L2B products.

The M1-temperature-dependent bias correction method was not available in time for the early FM-B period OSE and in lieu of this a reasonable bias correction of the HLOS winds as a function of geolocation (argument of latitude and longitude) using a look-up table of the past week's O–B departures was applied. It was shown that the M1-temperature-dependent bias correction method is better than the look-up table method, due to its scene dependence, benefitting the NWP impact in the mid-2020 OSE. Given the dominant source of bias has been removed, the DISC is focusing on resolving further much smaller bias sources.

Aeolus changed the analysis with some consistent patterns for different OSE periods. Rayleigh-clear wind assimilation led to systematic changes in the tropical zonal wind (peaking at around 100–150 hPa) that persist throughout the forecasts (whilst not making the mean departure from radiosondes worse). The transient changes in the analysis wind field due to Aeolus are largest in the various convergence zones around the world, and particularly so in the ITCZ. This suggests that Aeolus is mostly correcting winds associated with convection. Cases of discrepancies between Aeolus and background HLOS winds of greater than $10\,\mathrm{m\cdot s^{-1}}$ around the top of convective features have been found on several occasions. It is unclear if Aeolus' larger wind increments in convective areas are due to the inherent unpredictability of convection, or model errors from imperfect parametrization, or too-low resolution.

The Aeolus OSEs have all shown improvements in the short-range forecast fit to most other observation types sensitive to wind, temperature and humidity. This is considered to be a very reliable demonstration that Aeolus is improving the analysis and short-range forecasts. The relative impact of Aeolus on short-range forecasts was qualitatively compared to other ECMWF OSEs in recent years and found to be similar in magnitude to that of GPSRO (this has changed since COSMIC-2 became available in 2020, see Ruston and Healy (2020)), infrared radiances and AMVs. This is somewhat contradictory to the FSOI results, which show AMVs and IR to have much stronger impact than Aeolus.

The impact of Aeolus on short to medium-range forecasts as verified against analyses has produced some consistent patterns for the different OSE periods. That is, reasonable magnitude positive impact has been demonstrated on forecasts of vector wind, temperature and humidity (and hence geopotential height), in particular for the tropics and polar regions. Impact is greatest in the tropical upper troposphere. The tropics were expected to be where Aeolus winds would provide the largest impact, due to dynamical arguments suggesting the importance of wind versus mass information due to the large tropical Rossby radius of deformation (Žagar *et al.*, 2004); and corroborated by the results using *in situ* wind observations in Horányi *et al.* (2015a). The impact of Aeolus in the mid-2020 period has similar geographical patterns to the early FM-B period, but smaller in magnitude, which we attribute to the increased Rayleigh-clear noise. The increase in Rayleigh noise may also explain why the FSOI results for 2020 show the global Mie-cloudy impact is rather similar to the Rayleigh-clear impact.

The humidity improvements are presumably via improved winds leading to better advection of humidity. This is the reverse effect to that described for the all-sky radiance assimilation results (Geer *et al.*, 2018), in which the assimilation of humidity and cloud-sensitive observations during the assimilation window leads to the model modifying the wind field at the start of the window, such that the humidity is advected better to improve the fit to humidity-sensitive observations.

The impact of Rayleigh-clear winds is larger than Mie-cloudy winds for the early FM-B period OSE. It is thought that the much superior sampling of the atmosphere for Rayleigh-clear winds is the reason, despite the larger noise. The Rayleigh-clear impact is larger in the tropics, whereas the Mie-cloudy impact tends to be relatively strong in the extratropics. The FSOI results corroborate the stronger extratropical Mie-cloudy impact.

Aeolus is a demonstration mission for which the ground-processing algorithms are regularly being improved and the data assimilation methods have much room for improvement. Therefore, with future reprocessed L2B datasets and future data assimilation methodology improvements we expect that the NWP impact of Aeolus to increase relative to what has been shown in this article. The improvements described in this article compare favourably with historical improvements from introducing new observation types, see Bauer *et al.* (2015).

6 | CONCLUSIONS

Aeolus – the first Doppler wind lidar in space mission – produces wind retrievals of sufficient quality to improve ECMWF's global NWP forecasts. It is a useful contribution to the global observing system and hence it has been operationally assimilated by ECMWF since 9 January 2020, just less than 17 months after launch.

The estimated precision of Aeolus L2B HLOS winds varies considerably with: geolocation; season; processing software version; processor settings; range-bin settings; and instrument performance. Typically it is 4.0–7.0 $m \cdot s^{-1}$ for the Rayleigh-clear and 2.8–3.6 $m \cdot s^{-1}$ for the Mie-cloudy winds; which is consistent with some other studies. Despite being significantly noisier than expected pre-launch expectations and given that the Rayleigh-clear HLOS winds do not meet the WMO OSCAR "threshold" in the UTLS, the Aeolus winds provide sufficient information content for a very useful impact.

The magnitude of the positive impact was found to be strongly dependent on the implementation of a bias correction of the HLOS winds aided by the ECMWF background. An explanation was found for a dominant source of bias, which varies on sub-orbital time-scales, by correlating the ECMWF O–B departure statistics with the satellite's housekeeping information. Biases were found to depend on the gradients in temperature across the instrument's primary (or M1) mirror (part of the telescope) which in turn depend on the top-of-atmosphere radiation and thermal control of the mirror.

A simple bias correction to the ECMWF background as a function of argument of latitude and longitude (look-up table) was found to work well. However, the more physically based bias correction using the NRT primary mirror temperature readings as predictors, as implemented in the operational ground processing chain, provides a better correction, which improves the impact.

OSEs have demonstrated a positive impact of Aeolus for two periods: early FM-B laser (August–December 2019) and the mid-2020 FM-B laser period. Good magnitude improvements in short-range forecast departures relative to various high quality *in situ* and satellite observation types sensitive to temperature, wind and humidity were evident in both OSE periods. Aeolus' impact on short-range forecasts is found to be of a similar magnitude to some other important satellite observing systems from separate OSEs at ECMWF over recent years, which is an encouraging result; especially when Aeolus accounts for less than 1% of the observations assimilated with higher than anticipated random error.

Operational FSOI results (i.e. short-range forecast impact) show Aeolus provides a strong impact per observation. The total FSOI for Aeolus is similar in magnitude to a hyperspectral IR sounder instrument, for example, IASI.

OSE analysis-based verification demonstrated improvement in forecasts out to the medium range. The positive impact mainly occurs in the tropics and in polar regions reaching the lower stratosphere. The largest positive impact is in the tropical upper troposphere (~2% improvement in RMS error for vector wind and temperature at day 2 to 3 forecast range). Significant impact in the tropical lower stratospheric temperatures is observed to 9 days. Impact of ~1% is found in the polar regions out to several days.

The early FM-B OSEs show that Rayleigh-clear winds provide most of the positive impact (particularly in the tropics). However, the 2020 operational FSOI results contradict this somewhat, showing the Mie-cloudy and Rayleigh-clear winds have similar impact. This may be partly due to the decreasing Rayleigh-clear impact with time as it became noisier.

There are consistent geographical patterns in how Aeolus assimilation modifies the analysis wind fields. For example, the largest transient changes to zonal and meridional wind tend to be in the climatological convergence zones around the globe (convective scenes). Very high altitude (1 hPa) transient changes in zonal wind appear to result from changes in the propagation of gravity waves from the troposphere to the stratosphere, associated with orography and convection, an indirect effect. The mean changes are consistently large in the tropical upper troposphere and lower stratosphere for zonal wind, and near the Poles.

ACKNOWLEDGEMENTS

This research is funded by the European Space Agency (ESA) in the framework of the activities of the Aeolus DISC (Data Innovation and Science Cluster) consortium. The presented work includes preliminary data (not fully calibrated/validated and not yet publicly released) of the Aeolus mission that is part of the European Space Agency (ESA) Earth Explorer Programme. This includes wind products from before the public data release in May 2020. The preliminary Aeolus wind products will be reprocessed including a significant L2B product wind bias reduction. The processor development, improvement and product reprocessing preparation are performed by the Aeolus DISC, which involves DLR, DoRIT, ECMWF, KNMI, CNRS, S&T, ABB and Serco, in close cooperation with the Aeolus PDGS. It should be noted that the topics of ECMWF NWP impact and monitoring of Aeolus are predominantly the work of M. Rennie and L. Isaksen. The remaining co-authors contributed significantly to descriptions of the L2B data quality, ALADIN performance and the M1-temperature-dependent bias correction. Thanks to

the many experts from the DISC and from ESA, particularly: Thomas Flament (Météo-France), Gert-Jan Marseille (KNMI), Alain Dabas (Météo-France), Dorit Huber (DoRIT), Anne Grete Straume (ESA), Jonas Von Bismarck (ESA) and Tommaso Parrinello (ESA) who provided a fruitful forum for discussion during the Aeolus mission so far. Thanks to Mohamed Dahoui (ECMWF) for advice and support on observation monitoring and to Bill Bell (ECMWF) for advice that inspired the detection of the M1-temperature-dependent bias.

AUTHOR CONTRIBUTIONS

Michael Rennie: Conceptualization; data curation; formal analysis; investigation; methodology; project administration; resources; software; validation; visualization; writing-original draft; writing-review and editing. **Lars Isaksen:** Conceptualization; data curation; formal analysis; funding acquisition; investigation; methodology; project administration; resources; software; supervision; validation; visualization; writing-original draft; writing-review and editing. **Fabian Weiler:** Investigation; validation; visualization. **Jos de Kloe:** Data curation; investigation; validation. **Thomas Kanitz:** Investigation; validation; visualization. **Oliver Reitebuch:** Investigation; project administration; supervision; validation; writing-review and editing.

ORCID

Michael P. Rennie https://orcid.org/0000-0001-5472-2437

REFERENCES

Abdalla, S., Isaksen, L., Janssen, P. and Wedi, N. (2013) Effective spectral resolution of ECMWF atmospheric forecast models. *ECMWF Newsletter*, 137, 19–22. https://doi.org/10.21957/rue4o7ac.

Andersson, E., Hollingsworth, A., Kelly, G., Lönnberg, P., Pailleux, J. and Zhang, Z. (1991) Global observing system experiments on operational statistical retrievals of satellite sounding data. *Monthly Weather Review*, 119, 1851–1864. https://doi.org/10.1175/1520-0493(1991)119%3C1851:GOSEOO%3E2.0.CO;2.

Baker, W.E., Atlas, R., Cardinali, C., Clement, A., Emmitt, G.D., Gentry, B., Hardesty, M., Källén, E., Kavaya, M.J., Langland, R., Ma, Z., Masutani, M., McCarty, W., Pierce, R.B., Pu, Z., Riishojgaard, L.P., Ryan, J., Tucker, S., Weissmann, M. and Yoe, J.G. (2014) Lidar-measured wind profiles: the missing link in the global observing system. *Bulletin of the American Meteorological Society*, 95(4), 543–564. https://doi.org/10.1175/bams-d-12-00164.1.

Bauer, P., Thorpe, A. and Brunet, G. (2015) The quiet revolution of numerical weather prediction. *Nature*, 525, 47–55. https://doi.org/10.1038/nature14956.

Bell, W., Candy, B., Atkinson, N., Hilton, F., Baker, N., Bormann, N., Kelly, G., Kazumori, M., Campbell, W.F. and Swadley, S.D. (2008) The assimilation of SSMIS radiances in numerical weather prediction models. *IEEE Transactions on Geoscience and Remote Sensing*, 46(4), 884–900. https://doi.org/10.1109/TGRS.2008.917335.

Bormann, N., Lawrence, H. and Farnan, J. (2019) Global observing system experiments in the ECMWF assimilation system. *ECMWF Technical Memorandum*, 839, 8–12. https://doi.org/10.21957/sr184iyz.

Cardinali, C. (2009) Monitoring the observation impact on the short-range forecast. *Quarterly Journal of the Royal Meteorological Society*, 135(638), 239–250. https://doi.org/10.1002/qj.366.

Dabas, A., Denneulin, M.L., Flamant, P., Loth, C., Garnier, A. and Dolfi-Bouteyre, A. (2008) Correcting winds measured with a Rayleigh Doppler lidar from pressure and temperature effects. *Tellus A*, 60(2), 206–215. https://doi.org/10.1111/j.1600-0870.2007.00284.x.

Dahoui, M. and McNally, T. (2017) Studying trends and variability of dramatic atmospheric events using long time series of NWP satellite monitoring statistics. *The 21st International TOVS Study Conference (ITSC21)*. https://cimss.ssec.wisc.edu/itwg/itsc/itsc21/proceedings/6p.07_dahoui.pdf

Desroziers, G., Berre, L., Chapnik, B. and Poli, P. (2005) Diagnosis of observation background and analysis-error statistics in observation space. *Quarterly Journal of the Royal Meteorological Society*, 131(613), 3385–3396. https://doi.org/10.1256/qj.05.108.

ECMWF. (2020) *Integrated forecast system documentation*. Available at: https://www.ecmwf.int/En/Publications/Ifs-Documentation [Accessed 15th December 2020].

ESA. (2008) *ADM-Aeolus science report, European Space Agency*. Available at: https://earth.esa.int/documents/10174/1590943/AEOL002.pdf [Accessed 15th December 2020].

ESA. (2016) *ADM-Aeolus mission requirements document*. ESA Report AE-RP-ESA-SY-001. Available at: https://earth.esa.int/eogateway/documents/20142/1564626/Aeolus-Mission-Requirements.pdf [Accessed 15th December 2020].

Geer, A., Lonitz, K., Weston, P., Kazumori, M., Okamoto, K., Zhu, Y., Liu, E., Collard, A., Bell, W., Migliorini, S., Chambon, P., Fourrié, N., Kim, M.-J., Köpken-Watts, C. and Schraff, C. (2018) All-sky satellite data assimilation at operational weather forecasting centres. *Quarterly Journal of the Royal Meteorological Society*, 144(713), 1191–1217. https://doi.org/10.1002/qj.3202.

Geiß, A., Lehmann, V., Leinweber, R., Reitebuch, O. and Weissmann, M. (2020) Validation of the Aeolus L2B product with operational radar wind profiler measurements. *Aeolus Cal/Val and Science Workshop 2020*. Available at: https://nikal.eventsair.com/QuickEventWebsitePortal/2nd-aeolus-post-launch-calval-and-science-workshop/aeolus

Haseler, J. (2004) *Early-delivery suite*. ECMWF Technical Memoranda 454. https://doi.org/10.21957/f3wtwz0h

Hollingsworth, A., Shaw, D.B., Lönnberg, P., Illari, L., Arpe, K. and Simmons, A.J. (1986) Monitoring of observation and analysis quality by a data assimilation system. *Monthly Weather Review*, 114(5), 861–879. https://doi.org/10.1175/1520-0493(1986)114<0861:mooaaq>2.0.co;2.

Horányi, A., Cardinali, C., Rennie, M.P. and Isaksen, L. (2015a) The assimilation of horizontal line-of-sight wind information into the ECMWF data assimilation and forecasting system. Part I: The assessment of wind impact. *Quarterly Journal of the Royal Meteorological Society*, 141(689), 1223–1232. https://doi.org/10.1002/qj.2430.

Horányi, A., Cardinali, C., Rennie, M.P. and Isaksen, L. (2015b) The assimilation of horizontal line-of-sight wind information into

the ECMWF data assimilation and forecasting system. Part II: The impact of degraded wind observations. *Quarterly Journal of the Royal Meteorological Society*, 141(689), 1233–1243. https://doi.org/10.1002/qj.2551.

Houchi, K., Stoffelen, A., Marseille, G.J. and De Kloe, J. (2010) Comparison of wind and wind shear climatologies derived from high-resolution radiosondes and the ECMWF model. *Journal of Geophysical Research*, 115(D22123). https://doi.org/10.1029/2009JD013196.

Illingworth, A.J., Battaglia, A., Bradford, J., Forsythe, M., Joe, P., Kollias, P., Lean, K., Lori, M., Mahfouf, J.F., Melo, S., Midthassel, R., Munro, Y., Nicol, J., Potthast, R., Rennie, M.P., Stein, T.H.M., Tanelli, S., Tridon, F., Walden, C.J. and Wolde, M. (2018) WIVERN: a new satellite concept to provide global in-cloud winds, precipitation, and cloud properties. *Bulletin of the American Meteorological Society*, 99(8), 1669–1687. https://doi.org/10.1175/bams-d-16-0047.1.

Isaksen, L., Bonavita, M., Buizza, R., Fisher, M., Haseler, J., Leutbecher, M. and Raynaud, L. (2010) *Ensemble of data assimilations at ECMWF*. ECMWF Technical Memorandum 636. https://doi.org/10.21957/obke4k60

Khaykin, S.M., Hauchecorne, A., Wing, R., Keckhut, P., Godin-Beekmann, S., Porteneuve, J., Mariscal, J. and Schmitt, J. (2020) Doppler lidar at Observatoire De Haute-Provence for wind profiling up to 75 km altitude: performance evaluation and observations. *Atmospheric Measurement Techniques*, 13(3), 1501–1516. https://doi.org/10.5194/amt-13-1501-2020.

Korhonen, T., Perttu, K., Pasanen, M. and Sillanpaa, A. (2008) Polishing and testing of the 1.5 m SiC M1 mirror of the ALADIN instrument on the ADM-Aeolus satellite of ESA. *Optical Fabrication, Testing, and Metrology III*, 7102, 710219. https://doi.org/10.1117/12.797730.

Langland, R.H. and Baker, N.L. (2004) Estimation of observation impact using the NRL atmospheric variational data assimilation adjoint system. *Tellus A*, 56(3), 189–201. https://doi.org/10.1111/j.1600-0870.2004.00056.x.

Lu, Q., Bell, W., Bauer, P., Bormann, N. and Peubey, C. (2011) Characterizing the FY-3A microwave temperature sounder using the ECMWF model. *Journal of Atmospheric and Oceanic Technology*, 28(11), 1373–1389. https://doi.org/10.1175/jtech-d-10-05008.1.

Lux, O., Wernham, D., Bravetti, P., McGoldrick, P., Lecrenier, O., Riede, W., D'Ottavi, A., de Sanctis, V., Schillinger, M., Lochard, J., Marshall, J., Lemmerz, C., Weiler, F., Mondin, L., Ciapponi, A., Kanitz, T., Elfving, A., Parrinello, T. and Reitebuch, O. (2020a) High-power and frequency-stable ultraviolet laser performance in space for the wind lidar on Aeolus. *Optics Letters*, 45, 1443–1446. https://doi.org/10.1364/OL.387728.

Lux, O., Lemmerz, C., Weiler, F., Marksteiner, U., Witschas, B., Rahm, S., Geiß, A. and Reitebuch, O. (2020b) Intercomparison of wind observations from the European Space Agency's Aeolus satellite mission and the ALADIN Airborne Demonstrator. *Atmospheric Measurement Techniques*, 13(4), 2075–2097. https://doi.org/10.5194/amt-13-2075-2020.

Malardel, S., Wedi, N., Deconinck, W., Diamantakis, M., Kuehnlein, C., Mozdzynski, G., Hamrud, M. and Smolarkiewicz, P. (2016) A new grid for the IFS. *ECMWF Newsletter*, 146, 23–28. https://doi.org/10.21957/zwdu9u5i.

Marseille, G.-J., Stoffelen, A. and Barkmeijer, J. (2008) Impact assessment of prospective spaceborne Doppler wind lidar observation scenarios. *Tellus A*, 60(2), 234–248. https://doi.org/10.1111/j.1600-0870.2007.00289.x.

Martin, A., Weissmann, M., Reitebuch, O., Rennie, M.P., Geiß, A. and Cress, A. (2021) A validation of Aeolus winds using radiosonde observations and numerical weather prediction model equivalents. *Atmospheric Measurement Techniques*, 14, 2167–2183. https://doi.org/10.5194/amt-14-2167-2021.

McNally, A.P. (2019) On the sensitivity of a 4D-Var analysis system to satellite observations located at different times within the assimilation window. *Quarterly Journal of the Royal Meteorological Society*, 145(723), 2806–2816. https://doi.org/10.1002/qj.3596.

Reitebuch, O. (2012) The spaceborne wind lidar mission ADM-Aeolus. In: *Atmospheric Physics*. Research Topics in Aerospace, Schumann U. (eds). Berlin, Heidelberg: Springer, https://doi.org/10.1007/978-3-642-30183-4_49.

Reitebuch, O., Huber, D. and Nikolaus, I. (2018) *ADM-Aeolus, Algorithm Theoretical Basis Document (ATBD), level 1B products*. Oberpfaffenhofen: DLR Available at: https://earth.esa.int/eogateway/documents/20142/37627/Aeolus-L1B-Algorithm-ATBD.pdf.

Reitebuch, O., Lemmerz, C., Lux, O., Marksteiner, U., Rahm, S., Weiler, F., Witschas, B., Meringer, M., Schmidt, K., Huber, D., Nikolaus, I., Geiß, A., Vaughan, M., Dabas, A., Flament, T., Stieglitz, H., Isaksen, L., Rennie, M.P., de Kloe, J., Marseille, G.J., Stoffelen, A., Wernham, D., Kanitz, T., Straume, A.G., Fehr, T., von Bismarck, J., Floberghagen, R. and Parrinello, T. (2020a) Initial assessment of the performance of the first wind lidar in space on Aeolus. *EPJ Web of Conferences*, 237, 01010. https://doi.org/10.1051/epjconf/202023701010.

Reitebuch, O., Krisch, I., Lemmerz, C., Lux, O., Marksteiner, U., Masoumzadeh, N., Weiler, F., Witschas, B., Bracci, F., Meringer, M., Schmidt, K., Huber, D., Nikolaus, I., Fabre, F., Vaughan, M., Reissig, K., Dabas, A., Flament, T., Lacour, A., Mahfouf, J.-F., Savli, M., Trapon, D., Abdalla, S., Isaksen, L., Rennie, M., Donovan, D., de Kloe, J., Marseille, G.-J., Stoffelen, A., Perron, G., Jupin-Langlois, S., Smeets, J., Veneziani, M., Bucci, S., Gostinicchi, G., Ehlers, F., Kanitz, T., Straume, A.-G., Wernham, D., von Bismarck, J., Bley, S., Fischer, P., De Laurentis, M. and Parrinello, T. Assessment of Aeolus performance and bias correction - results from the Aeolus DISC. Aeolus Cal/Val and Science Workshop 2020, (2020b). https://nikal.eventsair.com/QuickEventWebsitePortal/2nd-aeolus-post-launch-calval-and-science-workshop/aeolus.

Rennie, M.P. (2016) *Advanced monitoring of Aeolus winds*. Reading, UK: ESA Contract Report. ECMWF Available at: https://www.ecmwf.int/node/18014.

Rennie, M.P., Tan, D., Andersson, E., Poli, P., Dabas, A., De Kloe, J., Marseille, G.-J. and Stoffelen, A. (2020) *Aeolus Level-2B Algorithm Theoretical Basis Document*. ECMWF. https://confluence.ecmwf.int/display/AEOL/L2B+processor+documentation+and+datasets

Rennie, M.P. and Isaksen, L. (2020) *The NWP impact of Aeolus level-2B winds at ECMWF*. ECMWF Technical Memorandum 864. https://doi.org/10.21957/alift7mhr

Rodwell, M.J., Magnusson, L., Bauer, P., Bechtold, P., Bonavita, M., Cardinali, C., Diamantakis, M., Earnshaw, P., Garcia-Mendez, A., Isaksen, L., Källén, E., Klocke, D., Lopez, P., McNally, T., Persson, A., Prates, F. and Wedi, N. (2013) Characteristics of occasional poor medium-range weather forecasts for Europe. *Bulletin of the*

American Meteorological Society, 94(9), 1393–1405. https://doi.org/10.1175/bams-d-12-00099.1.

Ruston, B. and Healy, S. (2020) Forecast impact of FORMOSAT-7/COSMIC-2 GNSS radio occultation measurements. *Atmospheric Science Letters*, 22(3), e1019. https://doi.org/10.1002/asl.1019.

Šavli, M., de Kloe, J., Marseille, G.-J., Rennie, M.P., Žagar, N. and Wedi, N. (2019) The prospects for increasing the horizontal resolution of the Aeolus horizontal line-of-sight wind profiles. *Quarterly Journal of the Royal Meteorological Society*, 145(725), 3499–3515. https://doi.org/10.1002/qj.3634.

Stoffelen, A. (1999) A simple method for calibration of a scatterometer over the ocean. *Journal of Atmospheric and Oceanic Technology*, 16, 275–282. https://doi.org/10.1175/1520-0426(1999)016%3C0275:ASMFCO%3E2.0.CO;2.

Stoffelen, A., Marseille, G.-J., Bouttier, F., Vasiljevic, D., de Haan, S. and Cardinali, C. (2006) ADM-Aeolus Doppler wind lidar observing system simulation experiment. *Quarterly Journal of the Royal Meteorological Society*, 132(619), 1927–1947. https://doi.org/10.1256/qj.05.83.

Stoffelen, A., Benedetti, A., Borde, R., Dabas, A., Flamant, P., Forsythe, M., Hardesty, M., Isaksen, L., Källén, E., Körnich, H., Lee, T., Reitebuch, O., Rennie, M.P., Riishøjgaard, L.P., Schyberg, H., Straume, A.G. and Vaughan, M. (2020a) Wind profile satellite observation requirements and capabilities. *Bulletin of the American Meteorological Society*, 101, E2005–E2021. https://doi.org/10.1175/BAMS-D-18-0202.1.

Stoffelen, A., Vogelzang, J. and Marseille, G.-J. (2020b) *High resolution data assimilation guide*. EUMETSAT Doc. NWPSAF-KN-UD-008, v. 1.2. Available at: https://nwp-saf.eumetsat.int/site/download/documentation/scatterometer/reports/High_Resolution_Wind_Data_Assimilation_Guide_1.3.pdf

Straume, A.G., Rennie, M.P., Isaksen, L., de Kloe, J., Marseille, G.-J., Stoffelen, A., Flament, T., Stieglitz, H., Dabas, A., Huber, D., Reitebuch, O., Lemmerz, C., Lux, O., Marksteiner, U., Weiler, F., Witschas, B., Meringer, M., Schmidt, K., Nikolaus, I., Geiß, A., Flamant, P., Kanitz, T., Wernham, D., von Bismarck, J., Bley, S., Fehr, T., Floberghagen, R. and Parinello, T. (2020) ESA's space-based Doppler Wind Lidar mission Aeolus first wind and aerosol product assessment results. *EPJ Web of Conferences*, 237, 01007. https://doi.org/10.1051/epjconf/202023701007.

Sun, X.J., Zhang, R.W., Marseille, G.-J., Stoffelen, A., Donovan, D., Liu, L. and Zhao, J. (2014) The performance of Aeolus in heterogeneous atmospheric conditions using high-resolution radiosonde data. *Atmospheric Measurement Techniques*, 7(8), 2695–2717. https://doi.org/10.5194/amt-7-2695-2014.

Tan, D.G.H., Andersson, E., Fisher, M. and Isaksen, L. (2007) Observing-system impact assessment using a data assimilation ensemble technique: application to the ADM Aeolus wind profiling mission. *Quarterly Journal of the Royal Meteorological Society*, 133(623), 381–390. https://doi.org/10.1002/qj.43.

Tan, D.G.H., Andersson, E., de Kloe, J., Marseille, G.-J., Stffelen, A., Poli, P., Denneulin, M.L., Dabas, A., Huber, D., Reitebuch, O., Flamant, P., Le Rille, O. and Nett, H. (2008) The ADM-Aeolus wind retrieval algorithms. *Tellus A*, 60(2), 191–205. https://doi.org/10.1111/j.1600-0870.2007.00285.x.

Weiler, F., Kanitz, T., Wernham, D., Rennie, M.P., Huber, D., Schillinger, M., Saint-Pe, O., Bell, R., Parrinello, T. and Reitebuch, O. (2020) Characterization of dark current signal measurements of the ACCDs used on board the Aeolus satellite. *Atmospheric Measurement Techniques*, 14(7), 5153–5177. https://doi.org/10.5194/amt-14-5153-2021.

Weissmann, M. and Cardinali, C. (2007) Impact of airborne Doppler lidar observations on ECMWF forecasts. *Quarterly Journal of the Royal Meteorological Society*, 133(622), 107–116. https://doi.org/10.1002/qj.16.

Witschas, B., Lemmerz, C. and Reitebuch, O. (2012) Horizontal lidar measurements for the proof of spontaneous Rayleigh–Brillouin scattering in the atmosphere. *Applied Optics*, 51, 6207–6219. https://doi.org/10.1364/AO.51.006207.

Witschas, B., Lemmerz, C., Geiß, A., Lux, O., Marksteiner, U., Rahm, S., Reitebuch, O. and Weiler, F. (2020) First validation of Aeolus wind observations by airborne Doppler wind lidar measurements. *Atmospheric Measurement Techniques*, 13(5), 2381–2396. https://doi.org/10.5194/amt-13-2381-2020.

WMO. (2018) Rolling Review of Requirements and Statements of Guidance. Available at: http://www.wmo.int/pages/prog/www/OSY/GOS-RRR.html. and OSCAR database https://www.wmo-sat.info/oscar/variables/view/wind_horizontal

Žagar, N., Gustafsson, N. and Källén, E. (2004) Dynamical response of equatorial waves in four-dimensional variational data assimilation. *Tellus A*, 56, 29–46. https://doi.org/10.3402/tellusa.v56i1.14389.

How to cite this article: Rennie, M.P., Isaksen, L., Weiler, F., de Kloe, J., Kanitz, T. & Reitebuch, O. (2021) The impact of Aeolus wind retrievals on ECMWF global weather forecasts. *Quarterly Journal of the Royal Meteorological Society*, 1–32. Available from: https://doi.org/10.1002/qj.4142